Precision measurements of the Higgs boson decays in $e^+e^- \to Z(\ell\ell)H$ with $H \to WW^* \to \ell\nu\ell\nu$ at the FCC-ee

Gadi Ninio [1] Jan Eysermans [2] Liron Barak [1]

[1]Tel Aviv University, Tel Aviv-Yafo, Israel

[2]Massachusetts Institute of Technology, Boston, USA

gadininio@tauex.tau.ac.il jan.eysermans@cern.ch lironbarak1@tauex.tau.ac.il

Abstract

This note presents a feasibility study of the measurement of $\sigma(e^+e^- \to ZH) \times \mathcal{B}(H \to WW^*)$ in the fully leptonic $Z(\ell\ell)H$, $H \to WW^* \to \ell\nu\ell\nu$ (where $\ell = e, \mu$) final state at FCC-ee. The study uses Monte Carlo samples processed through a parameterized simulation of the IDEA detector concept. Separate analyses are performed for projected integrated luminosities of 10.8 ab^{-1} at $\sqrt{s}$ = 240 GeV and 3.12 ab^{-1} at $\sqrt{s}$ = 365 GeV. Events are reconstructed from four charged leptons (electrons and/or muons) and missing momentum, selected using kinematic requirements, and classified with boosted decision trees. A binned likelihood fit to the classifier output gives expected relative precisions of 3.09% and 7.33% at 240 and 365 GeV, respectively, and 2.90% for their combination.

Contents

1 Introduction **3**
- 1.1 Higgs boson production at FCC-ee . . . 3
- 1.2 Physics and experimental motivation . . . 4
- 1.3 Experimental status and projections . . . 4

2 IDEA detector concept and response modelling **5**
- 2.1 The IDEA detector concept . . . 5
- 2.2 Reconstructed objects and detector response . . . 6

3 Simulated Monte Carlo samples **7**

4 Preselection **7**

5 Event reconstruction **8**

6 ZZ-fusion suppression at $\sqrt{s}$ = 365 GeV **11**

7 Event selection **12**

8 Multivariate event classification **19**

9 Results **20**

10 Conclusions **22**

A Monte Carlo sample details **25**
A.1 Event generators and signal filtering 25
A.2 Background topologies 25

B Additional preselection distributions **27**

C Leptonic category composition **30**

D Signal decomposition and additional ZZ-fusion studies **32**
D.1 Effect of the lepton-pairing metric 32
D.2 Additional VBF suppression variables 33

E Supplementary kinematic distributions **37**

F BDT-based classification training and validation **42**

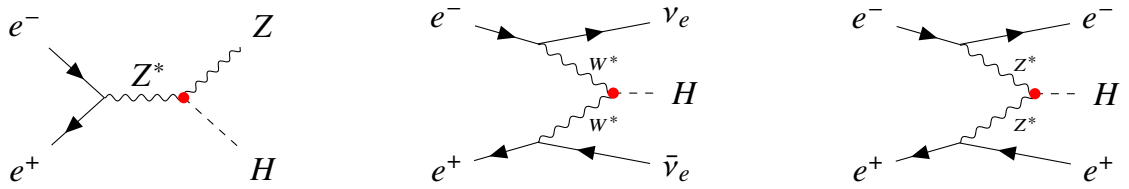
1 Introduction

Precision measurements of Higgs-boson properties are a central objective of the Future Circular Collider (FCC) physics programme [1–3]. This note presents a feasibility study of the $e^+e^- \to ZH$ process in the fully leptonic final state $Z(\ell\ell)H$, $H \to WW^* \to \ell\nu\ell\nu$, with $\ell = e, \mu$, at the FCC-ee operating energies of $\sqrt{s} = 240$ and 365 GeV. The reconstructed $Z \to \ell\ell$ candidate provides access to the recoil mass, while the Higgs-boson decay yields two additional charged leptons and missing momentum from the neutrinos.

This note is organized as follows. The remainder of this section summarizes Higgs production at FCC-ee, motivates the measurement, and reviews the current experimental status. The IDEA detector response and simulated samples are described in Sections 2 and 3. Section 4 and 5 present the event preselection and reconstruction, including the lepton pairing procedure and event categorization. The ZH, ZZ-fusion, and interference contributions at 365 GeV are discussed in Section 6. The optimized event selections are listed in Section 7. The multivariate classification and expected precision are reported in Sections 8 and 9, followed by the conclusions in Section 10.

1.1 Higgs boson production at FCC-ee

The FCC-ee Higgs programme is based primarily on Higgsstrahlung, $e^+e^- \to ZH$, and vector boson fusion (VBF) production. The latter includes WW-fusion, $e^+e^- \to \nu_e\bar{\nu}_e H$, and the smaller ZZ-fusion process, $e^+e^- \to e^+e^- H$. Their leading-order Feynman diagrams are shown in Figure 1.



(a) Higgsstrahlung: $e^+e^- \to ZH$ (b) WW-fusion: $e^+e^- \to \nu_e\bar{\nu}_e H$ (c) ZZ-fusion: $e^+e^- \to e^+e^- H$

Figure 1: Leading-order Feynman diagrams for the Higgs-boson production mechanisms at the FCC-ee: Higgsstrahlung (ZH) and the two VBF processes, WW-fusion and ZZ-fusion. The red dot marks the Higgs-boson production vertex.

The production cross sections have different centre-of-mass-energy dependences. The Higgsstrahlung cross section rises above the $m_Z + m_H \simeq 216$ GeV threshold, reaches its maximum near 255 GeV, and then decreases approximately as $1/s$. The VBF cross sections, on the other hand, increase approximately as $\ln(s/m_V^2)$, where m_V is the mass of the exchanged vector boson. Although the ZH cross section peaks near 255 GeV, the higher instantaneous luminosity achievable at 240 GeV more than compensates for the smaller cross section, making 240 GeV the preferred operating point for maximizing the expected Higgsstrahlung event rate. The 365 GeV stage, motivated primarily by the top-quark physics programme, provides a complementary Higgs dataset with a larger VBF contribution relative to ZH than at 240 GeV. Table 1 summarizes the inclusive production cross sections and expected numbers of Higgs bosons for projected integrated luminosities of 10.8 ab^{-1} at 240 GeV and 3.12 ab^{-1} at 365 GeV.

Higgsstrahlung is the target production mode of this analysis at both energies, with the Z boson decaying leptonically and the Higgs boson decaying as $H \to WW^* \to \ell\nu\ell\nu$. In the $Z \to e^+e^-$ channel, the same four-lepton final state is also produced through ZZ-fusion. Consequently, the electron-channel MC signal sample contains the Higgsstrahlung and ZZ-fusion amplitudes, together with their interference. The additional ZZ-fusion-plus-interference contribution is small at 240 GeV

Table 1: Approximate Higgs-production cross sections and expected event yields at the two FCC-ee operating energies considered in this note. The yields are calculated from the quoted cross sections and integrated luminosities [1]. The Higgsstrahlung contribution is quoted separately. The cross sections for the VBF processes include the corresponding contribution from interference with the Higgsstrahlung process. In particular, the WW-fusion entry includes interference with ZH, $Z \to \nu_e \bar{\nu}_e$, while the ZZ-fusion entry includes interference with ZH, $Z \to e^+e^-$.

	$\sqrt{s}$ = 240 GeV, $\mathcal{L}$ = 10.8 ab^{-1}		$\sqrt{s}$ = 365 GeV, $\mathcal{L}$ = 3.12 ab^{-1}	
Production mechanism	σ [fb]	Expected events	σ [fb]	Expected events
Higgsstrahlung, $e^+e^- \to ZH$	201	2.2×10^6	125	390×10^3
WW-fusion, $e^+e^- \to \nu_e \bar{\nu}_e H$	6.1	66×10^3	29.2	91×10^3
ZZ-fusion, $e^+e^- \to e^+e^- H$	0.4	4.3×10^3	3.2	10×10^3

but becomes non-negligible at 365 GeV. The event selection is therefore designed to suppress the non-Higgsstrahlung contribution and obtain a sample dominated by the targeted ZH process. The WW-fusion process does not contain an associated $Z \to \ell^+\ell^-$ decay and therefore does not contribute to the signal considered here.

1.2 Physics and experimental motivation

The $H \to WW^*$ branching fraction is approximately 21.5% [4], the second-largest decay branching fraction of the Standard Model (SM) Higgs boson. The measurement of $\sigma_{ZH} \times \mathcal{B}(H \to WW^*)$ constrains the combination $g^2_{HZZ} g^2_{HWW}/\Gamma_H$ and therefore provides an important input to the determination of g_{HWW} and Γ_H within the global Future Circular Collider electron–positron collider (FCC-ee) Higgs programme. In particular, it complements the inclusive ZH measurement [5] and other exclusive Higgs-decay measurements [6] in the FCC-ee coupling fit.

At a hadron collider, the unknown longitudinal momentum of the colliding partons and the two undetected neutrinos restrict the available kinematic information. At FCC-ee, the nominal initial state is known, enabling the use of the full three-dimensional missing momentum and the recoil against the reconstructed $Z \to \ell\ell$ candidate. The recoil mass is calculated from the nominal centre-of-mass energy $\sqrt{s}$ and the measured Z-candidate four-momentum:

$$m^2_{\text{rec}} = (\sqrt{s} - E_{\ell\ell})^2 - |\vec{p}_{\ell\ell}|^2 = s + m^2_{\ell\ell} - 2\sqrt{s}E_{\ell\ell}, \tag{1}$$

where $E_{\ell\ell}$, $\vec{p}_{\ell\ell}$, and $m_{\ell\ell}$ describe the reconstructed Z-candidate dilepton system. For correctly reconstructed ZH events, the recoil mass peaks near the Higgs-boson mass independently of its decay mode. A complementary estimate of the Higgs-boson mass is obtained by combining the two W-candidate leptons with the reconstructed missing four-momentum, providing additional signal–background discrimination.

The target signal is characterized by four prompt, isolated electrons or muons and missing momentum. Experimentally, the channel tests the tracking resolution relevant to the recoil mass, the acceptance and identification efficiency for the softest lepton, and the detector hermeticity required for missing-momentum reconstruction.

1.3 Experimental status and projections

The ATLAS and CMS collaborations have measured the $H \to WW^*$ decay in several Higgs-boson production modes, including gluon-gluon fusion (ggF), VBF, and associated production with vector

bosons [7, 8]. In particular, both collaborations have measured ZH production in the $H \to WW^*$ decay channel using combined three- and four-lepton final states. Using 140 fb^{-1} of 13 TeV data, ATLAS measured $\sigma_{ZH} \times \mathcal{B}(H \to WW^*) = 310^{+90}_{-80}$ (stat.) $\pm$ 30 (syst.) fb [9], compared with the SM expectation of 189^{+9}_{-8} fb [10]. CMS obtained 190^{+120}_{-100} (stat.)$^{+30}_{-20}$ (syst.) fb with 138 fb^{-1} of 13 TeV Run-2 data and 320^{+230}_{-180} (stat.)$^{+60}_{-30}$ (syst.) fb with 62 fb^{-1} of 13.6 TeV Run-3 data [11]. These ZH measurements remain statistically limited and provide an experimental benchmark for this channel.

Similar studies have been performed for other proposed electron–positron Higgs factories. At the ILC, a full-simulation study of the fully hadronic $Z(q\bar{q})H(WW^* \to 4q)$ final state at $\sqrt{s} = 250$ GeV obtained an expected relative statistical precision of 4.1% on $\sigma_{ZH} \times \mathcal{B}(H \to WW^*)$, assuming 500 fb^{-1} of integrated luminosity and polarized beams [12]. At the CEPC, the $H \to WW^*$ decay with hadronically decaying W bosons has been investigated in $Z(\mu^+\mu^-)H$ production at $\sqrt{s} = 240$ GeV, as part of a broader study of Higgs-boson branching-fraction measurements [13].

Existing FCC-ee studies have also evaluated the sensitivity to $H \to WW^*$ at $\sqrt{s} = 240$ GeV, so far focusing on hadronic W-boson decays. The $Z(\nu\nu)H[W(jj)W(jj)]$ channel is expected to reach a relative precision of 1.3% on $\sigma_{ZH} \times \mathcal{B}(H \to WW^*)$ [6], while a dedicated $Z(\ell\ell)H[W(jj)W(jj)]$ analysis based on a likelihood fit to the recoil-mass distribution obtains a precision of 1.6% [14]. A simultaneous analysis of $H \to WW^*$ and $H \to ZZ^*$ in the fully hadronic $Z(jj)H$ final state yields an expected precision of 1.48% on the $H \to WW^*$ contribution [15]. Combining these channels gives an expected precision of approximately 0.83% on $\sigma_{ZH} \times \mathcal{B}(H \to WW^*)$ at $\sqrt{s} = 240$ GeV [16]. The fully leptonic $H \to WW^* \to \ell\nu\ell\nu$ final state has not been considered in these projections and is the subject of this note.

2 IDEA detector concept and response modelling

To translate the massive collision rate and clean event topologies into precise physical measurements, the experimental apparatus must meet stringent performance requirements. This section first describes the physical design of the proposed IDEA detector. It then presents the parameterized detector response and the reconstructed physics objects used in this study.

2.1 The IDEA detector concept

The IDEA detector concept [17] is a general-purpose detector proposed for the FCC-ee, with overall dimensions of approximately 11×11 m in length and height. The most relevant capabilities for this fully leptonic $H \to WW^*$ study are precise charged-particle tracking over a broad momentum range, electron and muon identification, and sufficient detector hermeticity for reliable missing-momentum reconstruction.

The tracking system combines an ultra-light silicon vertex detector, a large low-mass drift chamber, and an outer silicon wrapper inside a 2 T magnetic field. The vertex detector comprises five barrel layers and three disks in each endcap, with a single-point resolution of a few micrometres. The surrounding drift chamber is approximately 4 m long and contains 112 measurement layers between radii of 35 and 200 cm. Its transverse material budget is about 1.6% of a radiation length. The outer silicon wrapper provides an additional precise measurement at the end of the tracking lever arm. This combination of low material and a large tracking volume supports precise momentum measurements over a broad kinematic range.

The calorimeter system consists of a segmented crystal electromagnetic calorimeter located inside the superconducting solenoid, followed by a dual-readout fibre calorimeter outside the coil. The inner crystal system measures electrons and photons before they traverse the solenoid material, while the fibre calorimeter measures both electromagnetic and hadronic shower components and

targets a stochastic hadronic energy resolution of approximately $30\%/\sqrt{E/\mathrm{GeV}}$. Their angular coverage and segmentation provide the calorimetric information used in particle-flow and missing-momentum reconstruction.

Muon identification is provided by three layers of micro-pattern gaseous detectors embedded in the magnetic flux-return yoke. These chambers supplement the inner tracking with measurements of particles penetrating the calorimeter system and provide a spatial resolution of a few hundred micrometres.

2.2 Reconstructed objects and detector response

The detector response and reconstructed analysis objects are modelled with the parameterized fast-simulation framework described below.

Parameterized Fast Simulation Framework The feasibility study presented in this note relies on a parameterized fast simulation rather than a computationally intensive full simulation (GEANT4) of the finalised detector geometry. The generated events are processed through DELPHES [18], a framework designed for the fast simulation of generic collider detectors. The specific configuration used for the samples in this note is the IDEA card from the `winter2023` branch of the FCC configuration repository ("`card_IDEA.tcl`") [19]. The `winter2023` configuration differs from the current IDEA detector concept in details of the vertex-detector geometry and in the placement of the solenoid relative to the calorimeters.

The expected detector response is modelled by passing stable generated particles through an ordered pipeline of parameterized response modules. First, charged particles are propagated through the modelled 2 T magnetic field to establish their expected trajectories. Next, particles are probabilistically retained or discarded based on their geometric acceptance and parameterized reconstruction efficiencies. The kinematic properties of the surviving particles are then smeared according to the expected vertex, tracking, and calorimetric resolutions. Finally, these parameterized tracks and energy deposits are fed into the reconstruction algorithms to obtain the high-level physics objects utilised in this analysis. By employing this framework, large signal and background datasets can be generated rapidly while retaining the leading physical effects of the detector response.

Electrons and Muons Electron and muon identification is based on the generator-level particle identity associated with each reconstructed charged-particle track. The track parameters are smeared using a covariance model derived from the expected vertex-detector and drift-chamber resolutions. Within the detector acceptance, the baseline tracking efficiency is set to unity, while a flat identification efficiency of 99% is assumed for both electrons and muons.

Missing Momentum The particle-flow (PF) collection comprises reconstructed charged particles, including the identified electrons and muons, together with photons and neutral hadrons. The complete collection is used to calculate the lepton isolation and missing-momentum vector. The reconstructed missing-momentum vector is derived from the negative vector sum of all PF candidates retained by the parameterized detector simulation, $\vec{p}_{\mathrm{miss}} = -\sum_i \vec{p}_i$. The corresponding missing energy is defined as $E_{\mathrm{miss}} = \sqrt{s} - \sum_i E_i$, and the missing invariant mass as $m_{\mathrm{miss}} = \sqrt{E_{\mathrm{miss}}^2 - |\vec{p}_{\mathrm{miss}}|^2}$. Because the nominal initial three-momentum at an e^+e^- collider is exactly zero, all three spatial components of the momentum imbalance can be reliably exploited.

3 Simulated Monte Carlo samples

The analysis uses centrally produced Monte Carlo (MC) samples from the official FCC-ee *winter2023* campaign. Samples at $\sqrt{s} = 240$ and 365 GeV are normalized to integrated luminosities of 10.8 ab^{-1} and 3.12 ab^{-1}, respectively, using the available theoretical production cross sections and branching fractions. Signal and purely leptonic samples are generated with WHIZARD [20] interfaced to PYTHIA 6 [21], while the inclusive ZZ, WW, and $t\bar{t}$ samples are generated with PYTHIA 8 [22]. All samples are processed through the same parameterized simulation of the IDEA detector concept described in Section 2.

The target signal is Higgsstrahlung, $e^+e^- \to ZH$, with $Z \to e^+e^-$ or $\mu^+\mu^-$ and $H \to WW^* \to \ell\nu\ell\nu$ for $\ell = e, \mu$. At 240 GeV, dedicated samples generated directly in the fully leptonic final state are used. At 365 GeV, inclusive $H \to WW^*$ samples are filtered at generator level to select electron and muon decays of both W bosons. The electron-channel sample at 365 GeV contains the Higgsstrahlung, ZZ-fusion, and interference contributions discussed in Section 6.

The dominant background is ZZ production, particularly $ZZ \to \ell\ell\tau\tau$ with both tau leptons decaying leptonically, which provides four charged leptons and genuine missing momentum. The much larger inclusive WW sample can satisfy the topology when the W bosons decay leptonically with additional leptons reconstructed, for example, through the conversion of an initial-state radiation photon. Another possibility is through semileptonic decays when one or both W bosons decay hadronically, in association with a converted radiated photon. At 365 GeV, $t\bar{t}$ production provides an additional background when both W bosons decay leptonically and semileptonic heavy-flavour decays yield four charged leptons and neutrinos. Inclusive $e^+e^- \to e^+e^-$ and $\mu^+\mu^-$ samples are also considered, but do not survive the four-lepton requirement.

Considering only the Higgsstrahlung process targeted by this measurement, the muon-channel sample is used as the pure-ZH reference for both leptonic Z-decay channels, assuming lepton universality. The corresponding effective final-state cross sections are approximately 0.137 and 0.083 fb at 240 and 365 GeV, respectively. These values are several orders of magnitude smaller than the inclusive background cross sections: 1.36 (0.64) pb for ZZ and 16.4 (10.7) pb for WW at 240 (365) GeV, with an additional 0.80 pb $t\bar{t}$ contribution at 365 GeV.

For the projected integrated luminosities, these yield approximately 1482 and 260 expected signal events. The resulting *ultimate precisions*, defined as the ideal statistical limits assuming 100% signal acceptance and no background contribution, are approximately 2.60% and 6.20%, respectively.

The complete sample identifiers, cross sections, simulated event counts, generator configurations, and detailed background topologies are provided in Appendix A.

4 Preselection

This section describes the initial event requirements used to define a clean four-lepton candidate sample before reconstructing the Z and WW^* systems. Although the same baseline topology is targeted at both centre-of-mass energies, the harder kinematics and additional $t\bar{t}$ background at $\sqrt{s} = 365$ GeV require energy-specific lepton momentum and isolation requirements.

At 240 GeV, the fully leptonic final state is characterized by four prompt leptons. The preselection requires exactly four leptons ($n_e + n_\mu = 4$) with momentum $p > 5$ GeV. To be consistent with the $Z \to \ell\ell$ and $W \to \ell\nu$ decay chains, the events must contain two opposite-sign (OS) lepton pairs and at least one same-flavour lepton pair. The four leptons are ordered by decreasing momentum, with ℓ_1, ℓ_2, ℓ_3, and ℓ_4 denoting the leading, subleading, third, and fourth leptons, respectively. Guided by the distributions given in Appendix B, loose cuts on the lepton momenta are applied, mainly

to constrain the signal shape: $20 < p_{\ell_1} < 85$ GeV, $10 < p_{\ell_2} < 80$ GeV, $10 < p_{\ell_3} < 80$ GeV, and $5 < p_{\ell_4} < 75$ GeV.

At 365 GeV, the larger Lorentz boosts of the $Z \to \ell\ell$ and $H \to WW^*$ systems produce harder kinematic spectra than at 240 GeV. In addition, the $t\bar{t}$ production channel opens, introducing a new background, while the ZZ-fusion (VBF) production mode begins to contribute alongside Higgsstrahlung. The fundamental preselection follows the 240 GeV strategy, but the loose lepton momentum cuts are re-optimized to accommodate the harder kinematic spectra shown in Appendix B: $20 < p_{\ell_1} < 165$ GeV, $10 < p_{\ell_2} < 160$ GeV, $5 < p_{\ell_3} < 150$ GeV, and $5 < p_{\ell_4} < 150$ GeV.

To suppress the $t\bar{t}$ background at 365 GeV, a lepton isolation requirement is imposed. The lepton isolation variable, ISO_ℓ, is defined as the sum of the momenta of all reconstructed particles within a hollow cone defined by $0.1 < \Delta R < 0.5$ around the lepton, divided by the lepton momentum, and is required to satisfy $\mathrm{ISO}_\ell < 3.0$ (equivalent to $\log_{10}(\mathrm{ISO}_\ell) < 0.48$) for each of the four leptons. This selection rejects 86% of the $t\bar{t}$ contribution while retaining 93% of the signal. The isolation of the fourth (softest) lepton provides the clearest separation between the signal and the $t\bar{t}$ background and is therefore shown in Figure 2.[1] The complete set of four isolation distributions is provided in Appendix B.

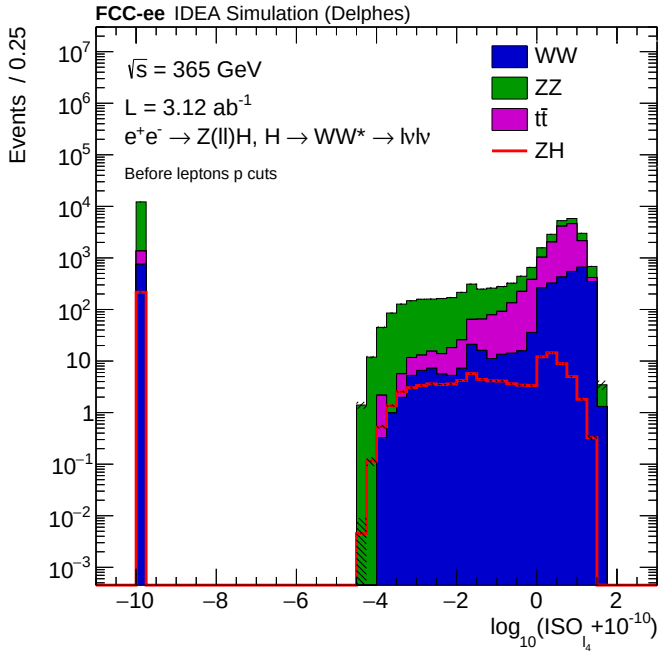


Figure 2: Distribution of the logarithm of the isolation for the fourth reconstructed lepton, $\log_{10}(\mathrm{ISO}_{\ell_4})$. All preselection requirements other than the lepton isolation and momentum requirements are applied. A value of 10^{-10} is added to the isolation observable to represent zero-isolation entries consistently on the logarithmic scale.

5 Event reconstruction

The four reconstructed leptons must be assigned to the Z- and WW^*-candidate systems, such that two leptons are assigned to the Z-boson candidate, while the remaining two define the WW^* candidate.

[1] The better signal and $t\bar{t}$ background separation observed in the fourth lepton isolation distribution is expected since the additional leptons in $t\bar{t}$ events can originate from heavy-flavour decays, and are therefore more frequently accompanied by nearby hadronic activity.

The lepton pairing is performed by minimizing a χ^2 metric that balances two kinematic constraints: the invariant mass of the Z-candidate leptons ($m_{\ell\ell}$) and the recoil mass (m_{rec}). For correctly reconstructed Higgsstrahlung events, these quantities are expected to peak near the Z-boson mass, $m_Z = 91.2$ GeV, and the Higgs-boson mass, $m_H = 125$ GeV, respectively. To control the relative contribution of these two constraints, the function is parametrized by a weight factor $f \in [0, 1]$:

$$\chi^2 = (1 - f)(m_{\ell\ell} - m_Z)^2 + f(m_{\text{rec}} - m_H)^2. \tag{2}$$

Once the same-flavour lepton pair that minimizes this χ^2 function is identified, the kinematic systems of the event can be explicitly reconstructed. The selected Z-candidate leading and subleading leptons are denoted as ℓ_{Z1} and ℓ_{Z2}, respectively, and their four-vector sum defines the reconstructed dilepton system, denoted as $Z \to \ell\ell$ (or simply $\ell\ell$), from which the recoil mass is computed. The remaining two leptons in the event are designated as the W-candidate leptons, similarly denoted as ℓ_{W1} and ℓ_{W2}, and their four-vector sum, combined with the missing momentum vector of the event, defines the reconstructed WW^* system.

The optimal value of f is not a fundamental physical quantity, but depends on both the experimental reconstruction performance and the kinematic properties of the event sample. In particular, it is affected by the lepton momentum and recoil-mass resolutions, as well as by whether the underlying production topology satisfies the two mass constraints. Therefore, to determine the optimal configuration for each operating energy, a scan over the parameter f is performed. For each value, the *lepton pairing efficiency* is evaluated. This efficiency is defined as the fraction of events where the selected W-candidate leptons match the true generator-level leptons originating from the WW^* system.[2]

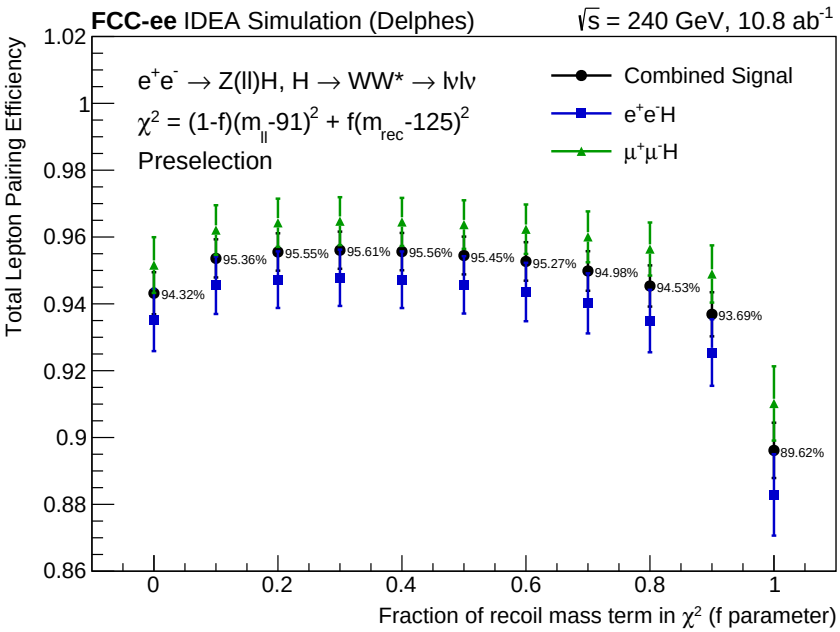
At $\sqrt{s} = 240$ GeV, the signal is dominated by the resonant Higgsstrahlung contribution, for which the invariant mass of the associated dilepton system is concentrated around the Z-boson mass. As shown in Figure 3a, the lepton pairing efficiency exhibits a broad maximum around $f = 0.2$–0.4, and $f = 0.4$ is adopted. This indicates that while the Z invariant mass is the dominant kinematic constraint (carrying a 60% weight), the recoil mass provides important supplementary information to resolve pairing ambiguities. The optimized χ^2 function is hence:

$$\chi^2_{240} = 0.6(m_{\ell\ell} - m_Z)^2 + 0.4(m_{\text{rec}} - m_H)^2. \tag{3}$$

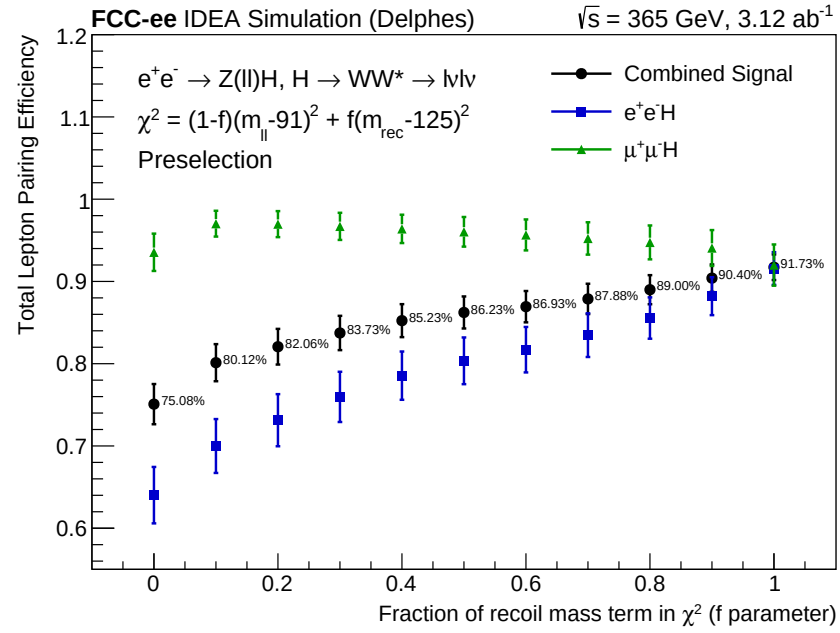
At $\sqrt{s} = 365$ GeV, the electron-channel event kinematics also receive a relatively small nonresonant ZZ-fusion contribution and its interference with Higgsstrahlung, whereas the muon channel contains only the Higgsstrahlung contribution. The two channels therefore exhibit opposite trends in the pairing efficiency as a function of f. For the muon channel, the $m_{\ell\ell}$ term provides useful information for identifying the resonant $Z \to \mu\mu$ decay, and the pairing efficiency decreases as the recoil-mass term is given greater weight. In contrast, the inclusive electron-channel efficiency increases with f, since the nonresonant ZZ-fusion contribution does not contain a $Z \to ee$ resonance and an $m_{\ell\ell} \simeq m_Z$ constraint can therefore favour incorrect pairings for these events. As illustrated in Figure 3b, the combined signal pairing efficiency is highest for $f = 1.0$. Although the ZZ-fusion contribution does not contain a resonant $Z \to ee$ decay, the recoil mass computation does not require such a resonance. This value is adopted despite the modest loss in Higgsstrahlung pairing efficiency, since removing the $m_{\ell\ell}$ term avoids artificially pulling the nonresonant component towards the Z-boson mass and therefore allows it to be efficiently suppressed, as discussed in Section 6. The resulting pairing metric depends only on the recoil mass:

$$\chi^2_{365} = (m_{\text{rec}} - m_H)^2.$$

[2]Specifically, the W-candidate leptons are matched, rather than the Z-candidate leptons, since the lepton pair is generated inclusively. Therefore, there is no intermediate Z boson explicitly recorded in the generator-level event history.



(a) $\sqrt{s}$ = 240 GeV



(b) $\sqrt{s}$ = 365 GeV

Figure 3: Lepton pairing efficiency as a function of the recoil-mass weight f in the pairing χ^2 at (a) $\sqrt{s}$ = 240 GeV and (b) $\sqrt{s}$ = 365 GeV. Results are shown for the combined signal sample (circle markers) and separately for the electron (square markers) and muon (triangle markers) channels. At 240 GeV, the efficiency exhibits a broad maximum around f = 0.2–0.4; at 365 GeV, it improves steadily as the recoil-mass term receives greater weight.

Events can then be divided into six flavour categories according to the reconstructed Z- and WW^*-candidate leptons: $4e$, 4μ, $2e2\mu$, $2\mu2e$, $3e1\mu$, and $3\mu1e$, where the first pair denotes the Z-candidate leptons. Such categorization could improve the sensitivity if the different leptonic final-state categories exhibit distinct kinematic properties or background compositions, or if observables such as the dilepton and recoil masses have different resolutions across the categories. However, this study reveals similar overall event kinematics and signal-to-background ratios across the six channels. Therefore, to preserve statistical power in the individual bins and to simplify the overall analysis architecture, all subsequent event selection, multivariate analysis, and signal extraction procedures are performed inclusively across all leptonic configurations. The different lepton flavour composition distributions are provided in Appendix C.

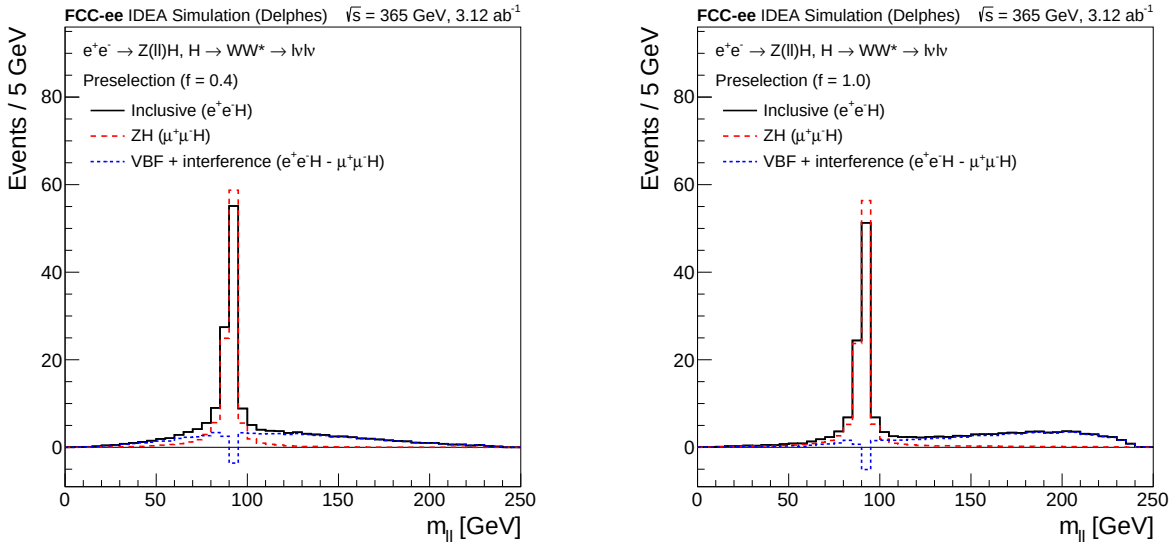
6 ZZ-fusion suppression at $\sqrt{s} = 365$ GeV

At $\sqrt{s} = 365$ GeV, the $e^+e^- \to e^+e^-H$ final state receives contributions from Higgsstrahlung, ZZ-fusion, and their interference. The $e^+e^- \to \mu^+\mu^-H$ channel, by contrast, is populated only by Higgsstrahlung. Before filtering the W-boson decays, the generated $H \to WW^*$ cross sections are 1.590 fb for the electron channel and 0.9007 fb for the muon channel. Assuming lepton universality for the ZH contribution, the muon-channel value provides the Higgsstrahlung expectation for the electron channel, while their difference, 0.689 fb, represents the ZZ-fusion-plus-interference contribution in the generated sample. Accordingly, the difference between the electron- and muon-channel distributions is used to study the ZZ-fusion-plus-interference component:

$$\left(e^+e^- \to e^+e^-H\right) - \left(e^+e^- \to \mu^+\mu^-H\right). \tag{4}$$

This subtraction does not isolate pure ZZ-fusion because the interference contribution remains included.

When applying the 240 GeV pairing configuration ($f = 0.4$) to the 365 GeV sample, the dilepton-mass term in the pairing metric tends to pull nonresonant electron pairs, including those associated with the ZZ-fusion-plus-interference contribution, towards the nominal Z-boson mass, as shown in Figure 4a. However, for $f = 1.0$ the dilepton-mass term is removed from the pairing metric. The resonant ZH contribution remains concentrated around m_Z, while most of the nonresonant ZZ-fusion-plus-interference component is reconstructed at larger dilepton masses, as shown in Figure 4b. Consequently, requiring $m_{\ell\ell} < 111$ GeV rejects approximately 95% of this component while retaining approximately 89% of the ZH signal. Additional ZZ-fusion suppression studies are provided in Appendix D.



(a) $f = 0.4$ pairing

(b) $f = 1.0$ pairing

Figure 4: Reconstructed dilepton invariant-mass distributions obtained with the (a) $f = 0.4$ and (b) $f = 1.0$ pairing schemes at $\sqrt{s} = 365$ GeV. The inclusive electron channel (solid line), the muon-channel ZH proxy (dashed line), and their difference – corresponding to the ZZ-fusion-plus-interference component (dotted line) – are shown.

7 Event selection

Kinematic requirements are applied to enhance the Higgsstrahlung signal relative to the background processes.

At $\sqrt{s} = 240$ GeV, the following event selections are applied:

- $Z \to \ell\ell$ **system:** The invariant mass is restricted to $|m_{\ell\ell} - m_Z| < 15$ GeV, and the dilepton momentum must fall within $20 < p_{\ell\ell} < 70$ GeV.
- **Recoil mass:** The recoil mass is required to be $120 < m_{\text{rec}} < 145$ GeV to remain consistent with the expected Higgs boson mass peak.
- **Missing energy:** To ensure that the missing momentum vector points safely within the tracker acceptance, we require $|\cos\theta_{\text{miss}}| < 0.98$. Alongside this geometric constraint, to target the two escaping neutrinos an energy requirement of $20 < E_{\text{miss}} < 120$ GeV is applied.
- WW^* **system:** The reconstructed invariant mass must satisfy $60 < m_{WW^*} < 135$ GeV, and the angular separation between the W-candidate leptons is required to be $\Delta R(\ell_{W1}, \ell_{W2}) > 0.25$ to reduce the WW background.

At $\sqrt{s} = 365$ GeV, to mitigate the enhanced $t\bar{t}$ and WW backgrounds and adapt to the higher system boosts, the selections are re-optimized and two additional requirements are introduced:

- $Z \to \ell\ell$ **system:** $|m_{\ell\ell} - m_Z| < 20$ GeV and a shifted momentum range of $35 < p_{\ell\ell} < 155$ GeV. The angular separation between the Z-candidate leptons is constrained to $\Delta R(\ell_{Z1}, \ell_{Z2}) < 3.0$ to reduce the WW background.
- **Recoil mass:** Broadened to $115 < m_{\text{rec}} < 230$ GeV.

- **Missing energy:** The geometric requirement $|\cos\theta_{\text{miss}}| < 0.98$ is kept, while the energy window is significantly broadened to $20 < E_{\text{miss}} < 180$ GeV to accommodate the higher system boost.
- WW^* **system:** Broadened to $m_{WW^*} > 50$ GeV and an angular-separation window of $0.1 < \Delta R(\ell_{W1}, \ell_{W2}) < 4.0$.
- **Systems separation:** The angular separation between the Z system and the WW^* system is required to be $\Delta R(Z \to \ell\ell, WW^*) > 3.0$ to ensure proper topological separation and suppress the remaining $t\bar{t}$ background.

Table 2: Optimized kinematic selections at the two centre-of-mass energies, applied after preselection and event reconstruction. A dash indicates that no requirement is applied.

Selection	240 GeV	365 GeV
$m_{\ell\ell}$ [GeV]	76–106	71–111
$p_{\ell\ell}$ [GeV]	20–70	35–155
m_{rec} [GeV]	120–145	115–230
$\lvert\cos\theta_{\text{miss}}\rvert$	< 0.98	< 0.98
E_{miss} [GeV]	20–120	20–180
m_{WW^*} [GeV]	60–135	> 50
$\Delta R(\ell_{W1}, \ell_{W2})$	> 0.25	0.1–4.0
$\Delta R(\ell_{Z1}, \ell_{Z2})$	—	< 3.0
$\Delta R(Z \to \ell\ell, WW^*)$	—	> 3.0

Table 3: Cutflow for the signal and background samples at $\sqrt{s} = 240$ GeV. Event yields are given for an integrated luminosity of 10.8 ab^{-1}; the value in parentheses is the efficiency of each requirement relative to the preceding selection. The lepton momentum requirements are $20 < p_{\ell_1} < 85$ GeV, $10 < p_{\ell_2} < 80$ GeV, $10 < p_{\ell_3} < 80$ GeV, and $5 < p_{\ell_4} < 75$ GeV, where the leptons are ordered by decreasing momentum. The total efficiencies are expressed as dimensionless fractions. The final row shows the fractional composition of the final total signal and background yields.

		Signal			Background		
Selection	$S/\sqrt{S+B}$	eeH	$\mu\mu H$	Total signal	ZZ	WW	Total Background
All events	0.1	7.86×10^{2} (100.0%)	7.41×10^{2} (100.0%)	1.53×10^{3} (100.0%)	1.47×10^{7} (100.0%)	1.78×10^{8} (100.0%)	1.92×10^{8} (100.0%)
Four leptons	3.5	6.97×10^{2} (88.6%)	6.61×10^{2} (89.2%)	1.36×10^{3} (88.9%)	1.39×10^{5} (0.9%)	9.11×10^{3} (0.0051%)	1.48×10^{5} (0.1%)
Two OS pairs	3.6	6.97×10^{2} (100.0%)	6.61×10^{2} (100.0%)	1.36×10^{3} (100.0%)	1.32×10^{5} (94.8%)	8.69×10^{3} (95.5%)	1.41×10^{5} (94.8%)
At least one same-flavour pair	3.6	6.97×10^{2} (100.0%)	6.61×10^{2} (100.0%)	1.36×10^{3} (100.0%)	1.32×10^{5} (100.0%)	8.69×10^{3} (100.0%)	1.41×10^{5} (100.0%)
Lepton momentum	5.7	6.94×10^{2} (99.5%)	6.59×10^{2} (99.7%)	1.35×10^{3} (99.6%)	5.04×10^{4} (38.2%)	4.24×10^{3} (48.7%)	5.47×10^{4} (38.9%)
$76 < m_{\ell\ell} < 106$ GeV	6.3	6.26×10^{2} (90.2%)	6.22×10^{2} (94.4%)	1.25×10^{3} (92.3%)	3.73×10^{4} (73.9%)	7.47×10^{2} (17.6%)	3.80×10^{4} (69.5%)
$20 < p_{\ell\ell} < 70$ GeV	8.1	6.20×10^{2} (99.0%)	6.17×10^{2} (99.2%)	1.24×10^{3} (99.1%)	2.15×10^{4} (57.6%)	6.74×10^{2} (90.1%)	2.21×10^{4} (58.2%)
$120 < m_{\text{rec}} < 145$ GeV	10.4	6.03×10^{2} (97.4%)	6.07×10^{2} (98.3%)	1.21×10^{3} (97.8%)	1.20×10^{4} (55.9%)	4.18×10^{2} (62.0%)	1.24×10^{4} (56.1%)
$\lvert\cos\theta_{\text{miss}}\rvert < 0.98$	13.0	5.91×10^{2} (98.0%)	5.94×10^{2} (98.0%)	1.19×10^{3} (98.0%)	6.72×10^{3} (56.0%)	4.05×10^{2} (96.9%)	7.13×10^{3} (57.4%)
$20 < E_{\text{miss}} < 120$ GeV	22.4	5.91×10^{2} (100.0%)	5.94×10^{2} (100.0%)	1.19×10^{3} (100.0%)	1.22×10^{3} (18.2%)	3.87×10^{2} (95.5%)	1.61×10^{3} (22.6%)
$60 < m_{WW^*} < 135$ GeV	25.6	5.88×10^{2} (99.4%)	5.91×10^{2} (99.5%)	1.18×10^{3} (99.5%)	6.47×10^{2} (52.9%)	2.90×10^{2} (74.8%)	9.36×10^{2} (58.1%)
$\Delta R(\ell_{W1}, \ell_{W2}) > 0.25$	26.7	5.77×10^{2} (98.2%)	5.80×10^{2} (98.1%)	1.16×10^{3} (98.1%)	6.32×10^{2} (97.7%)	8.32×10^{1} (28.7%)	7.15×10^{2} (76.4%)
Total efficiency		0.734	0.783	0.758	4.3×10^{-5}	4.7×10^{-7}	3.7×10^{-6}
Composition		49.9%	50.1%	100.0%	88.4%	11.6%	100.0%

Table 4: Cutflow for the signal and background samples at $\sqrt{s} = 365$ GeV. The eeH signal sample contains the ZH, ZZ-fusion, and interference contributions, whereas the $\mu\mu H$ sample contains only the ZH contribution. Event yields are given for an integrated luminosity of 3.12 ab^{-1}; the value in parentheses is the efficiency of each requirement relative to the preceding selection. The lepton requirements are $\mathrm{ISO}_\ell < 3.0$ for every lepton and $20 < p_{\ell_1} < 165$ GeV, $10 < p_{\ell_2} < 160$ GeV, $5 < p_{\ell_3} < 150$ GeV, and $5 < p_{\ell_4} < 150$ GeV, where the leptons are ordered by decreasing momentum. The total efficiencies are expressed as dimensionless fractions. The final row shows the fractional composition of the final total signal and background yields.

		Signal			Background			
Selection	$S/\sqrt{S+B}$	eeH	$\mu\mu H$	Total signal	ZZ	WW	$t\bar{t}$	Total Background
All events	0.1	2.30×10^{2} (100.0%)	1.30×10^{2} (100.0%)	3.60×10^{2} (100.0%)	2.01×10^{6} (100.0%)	3.34×10^{7} (100.0%)	2.50×10^{6} (100.0%)	3.79×10^{7} (100.0%)
Four leptons	1.5	1.96×10^{2} (85.1%)	1.17×10^{2} (90.2%)	3.13×10^{2} (87.0%)	1.98×10^{4} (1.0%)	3.77×10^{3} (0.011%)	2.13×10^{4} (0.9%)	4.48×10^{4} (0.1%)
Lepton isolation	2.1	1.83×10^{2} (93.4%)	1.09×10^{2} (93.2%)	2.92×10^{2} (93.3%)	1.43×10^{4} (72.3%)	1.27×10^{3} (33.6%)	2.97×10^{3} (14.0%)	1.85×10^{4} (41.3%)
Two OS pairs	2.2	1.83×10^{2} (100.0%)	1.09×10^{2} (100.0%)	2.92×10^{2} (100.0%)	1.41×10^{4} (98.6%)	1.25×10^{3} (99.0%)	2.12×10^{3} (71.4%)	1.75×10^{4} (94.2%)
At least one same-flavour pair	2.2	1.83×10^{2} (100.0%)	1.09×10^{2} (100.0%)	2.92×10^{2} (100.0%)	1.41×10^{4} (100.0%)	1.25×10^{3} (100.0%)	2.12×10^{3} (100.0%)	1.75×10^{4} (100.0%)
Lepton momentum	2.3	1.83×10^{2} (100.0%)	1.09×10^{2} (100.0%)	2.92×10^{2} (100.0%)	1.20×10^{4} (85.0%)	1.19×10^{3} (95.1%)	2.03×10^{3} (95.4%)	1.52×10^{4} (87.0%)
$71 < m_{\ell\ell} < 111$ GeV	2.4	1.01×10^{2} (55.5%)	9.74×10^{1} (89.1%)	1.99×10^{2} (68.0%)	6.35×10^{3} (53.1%)	1.91×10^{2} (16.0%)	3.27×10^{2} (16.1%)	6.87×10^{3} (45.3%)
$35 < p_{\ell\ell} < 155$ GeV	2.9	1.01×10^{2} (99.6%)	9.72×10^{1} (99.8%)	1.98×10^{2} (99.7%)	4.04×10^{3} (63.7%)	1.80×10^{2} (94.1%)	2.77×10^{2} (84.7%)	4.50×10^{3} (65.5%)
$115 < m_{\mathrm{rec}} < 230$ GeV	3.4	9.74×10^{1} (96.3%)	9.41×10^{1} (96.8%)	1.92×10^{2} (96.6%)	2.89×10^{3} (71.4%)	1.23×10^{2} (68.2%)	5.55×10^{1} (20.0%)	3.07×10^{3} (68.1%)
$\lvert\cos\theta_{\mathrm{miss}}\rvert < 0.98$	4.3	9.55×10^{1} (98.1%)	9.25×10^{1} (98.3%)	1.88×10^{2} (98.2%)	1.56×10^{3} (54.0%)	1.18×10^{2} (96.5%)	5.45×10^{1} (98.3%)	1.73×10^{3} (56.5%)
$20 < E_{\mathrm{miss}} < 180$ GeV	7.4	9.47×10^{1} (99.2%)	9.17×10^{1} (99.1%)	1.86×10^{2} (99.2%)	2.89×10^{2} (18.5%)	1.06×10^{2} (89.4%)	5.45×10^{1} (100.0%)	4.50×10^{2} (25.9%)
$m_{WW^*} > 50$ GeV	8.2	9.41×10^{1} (99.3%)	9.11×10^{1} (99.3%)	1.85×10^{2} (99.3%)	1.94×10^{2} (67.1%)	9.23×10^{1} (87.3%)	3.88×10^{1} (71.2%)	3.25×10^{2} (72.3%)
$0.1 < \Delta R(\ell_{W1}, \ell_{W2}) < 4.0$	8.4	9.33×10^{1} (99.2%)	9.04×10^{1} (99.2%)	1.84×10^{2} (99.2%)	1.87×10^{2} (96.4%)	7.03×10^{1} (76.2%)	3.88×10^{1} (100.0%)	2.96×10^{2} (91.1%)
$\Delta R(Z \to \ell\ell, WW^*) > 3.0$	8.6	9.23×10^{1} (98.9%)	8.95×10^{1} (99.1%)	1.82×10^{2} (99.0%)	1.82×10^{2} (97.1%)	6.80×10^{1} (96.7%)	1.76×10^{1} (45.2%)	2.67×10^{2} (90.2%)
$\Delta R(\ell_{Z1}, \ell_{Z2}) < 3.0$	9.1	8.82×10^{1} (95.6%)	8.62×10^{1} (96.3%)	1.74×10^{2} (96.0%)	1.44×10^{2} (79.6%)	3.65×10^{1} (53.6%)	1.39×10^{1} (78.9%)	1.95×10^{2} (72.9%)
Total efficiency		0.384	0.663	0.484	7.2×10^{-5}	1.1×10^{-6}	5.6×10^{-6}	5.1×10^{-6}
Composition		50.6%	49.4%	100.0%	74.2%	18.7%	7.1%	100.0%

The complete selections for both centre-of-mass energies are summarized in Table 2. The evolution of the event yields is shown in Figures 5a and 5b; the corresponding cutflow tables are provided in Tables 3 and 4, for 240 and 365 GeV, respectively. At 240 GeV, the final signal selection efficiency is approximately 76%, while the overall background efficiency is 3.7×10^{-6}. For 10.8 ab^{-1}, these efficiencies correspond to expected signal and background yields of 1157 and 715 events, respectively, giving a statistical significance of $S/\sqrt{S+B} \approx 26.7$, where S and B denote the selected signal and background yields. At 365 GeV, the selections retain approximately 48% of signal (and specifically 66% of the ZH component), while the overall background efficiency is 5.1×10^{-6}. For 3.12 ab^{-1}, these efficiencies correspond to expected signal and background yields of 174 and 195 events, respectively, giving a statistical significance of $S/\sqrt{S+B} \approx 9.1$.

After the full selection, the background at 240 GeV is dominated by ZZ production (88%), with the remaining 12% arising from WW events. The main irreducible contribution is $ZZ \to \ell\ell\tau\tau$, where both tau leptons decay leptonically and therefore provide the required four charged leptons and genuine missing momentum. The selected yield from a dedicated fully leptonic WW sample is approximately a factor of two smaller than that from the inclusive WW sample, likely due to additional decay topologies that can mimic the signal final state, such as semileptonic heavy-flavour decays combined with conversions of radiated photons.

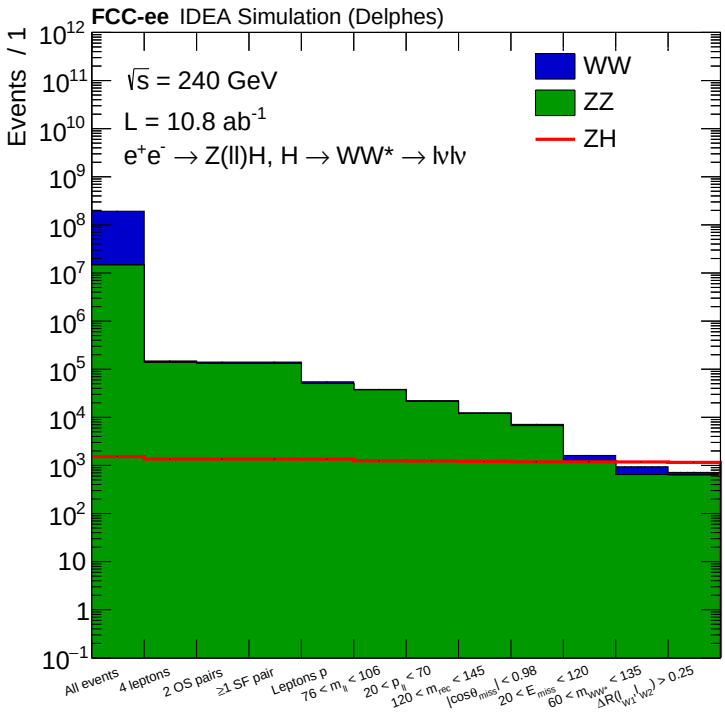
At 365 GeV, ZZ remains dominant (74%), while WW and $t\bar{t}$ account for 19% and 7% of the selected background, respectively. The $t\bar{t}$ contribution appears only above the top-pair production threshold, and can satisfy the signal topology when, e.g., the two top-quark W bosons decay leptonically and the two b-quark decay chains provide additional charged leptons and neutrinos via semileptonic decays. The specific WW and $t\bar{t}$ decay topologies capable of satisfying the four-lepton selection are described in Section 3.

Compared with the 240 GeV analysis, the 365 GeV analysis ultimately yields a less favorable signal-to-background ratio, $S/B \simeq 0.90$ rather than 1.62. This reflects the reduced selected signal yield relative to the remaining backgrounds, together with the opening of the $t\bar{t}$ production channel.

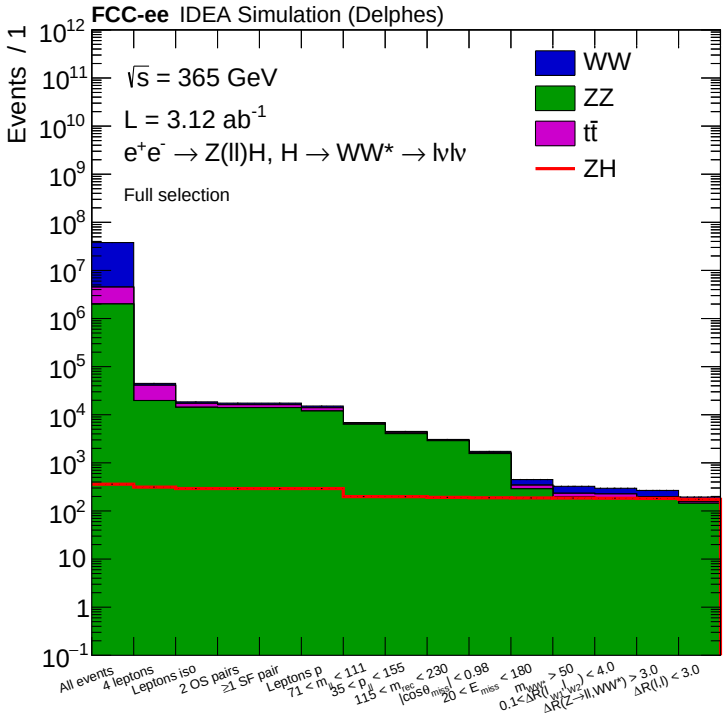
Two complementary observables reconstruct the Higgs-boson mass: the recoil mass inferred from the Z-candidate and the WW^* system invariant mass (m_{WW^*}) reconstructed from the two W-candidate leptons and the missing four-momentum. For correctly reconstructed ZH events, both observables are related to the Higgs-boson mass, whereas the backgrounds form broader distributions. In the recoil-mass distributions shown in Figures 6a and 6b, the signal distribution is asymmetric at both centre-of-mass energies, with a pronounced high-mass tail. Initial-state radiation and beamstrahlung can cause the incoming electron or positron to emit photons before the hard collision, reducing the actual hard-scattering energy $\sqrt{s'}$ below the nominal $\sqrt{s}$. Since the recoil mass is nevertheless computed using the nominal $\sqrt{s}$ value, these events are reconstructed at artificially larger recoil masses. Furthermore, the peak is broader at 365 GeV, since uncertainties in the Z-candidate dilepton energy have a larger propagated effect on the recoil mass, and the more energetic Z-candidate leptons are reconstructed with a larger absolute momentum uncertainty [23].

The reconstructed m_{WW^*} distributions in Figures 6c and 6d instead exhibit a broad asymmetric shape with a pronounced tail below the Higgs-boson mass. The missing momentum system consists of two neutrinos and therefore generally has a nonzero invariant mass, but its reconstructed four-vector is formed with the invariant mass set to zero. This causes m_{WW^*} to underestimate the true Higgs-boson mass and smears the distribution preferentially towards lower values.

A selected set of kinematic distributions with the optimized requirements applied is provided in Appendix E.

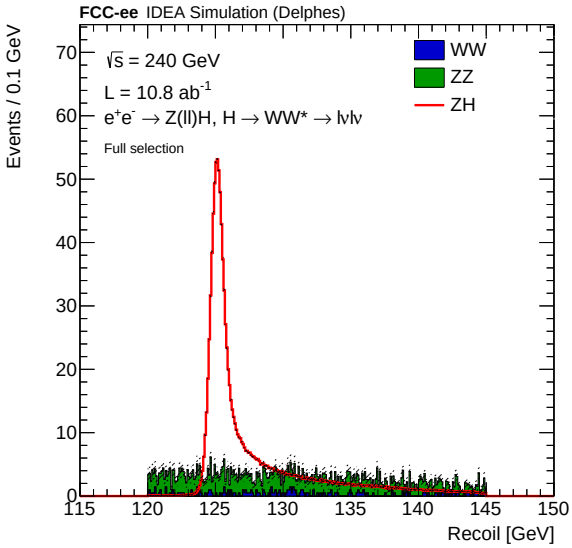


(a) $\sqrt{s}$ = 240 GeV

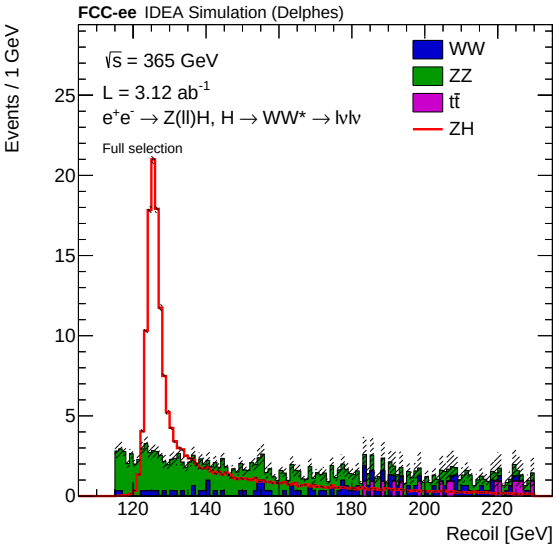


(b) $\sqrt{s}$ = 365 GeV

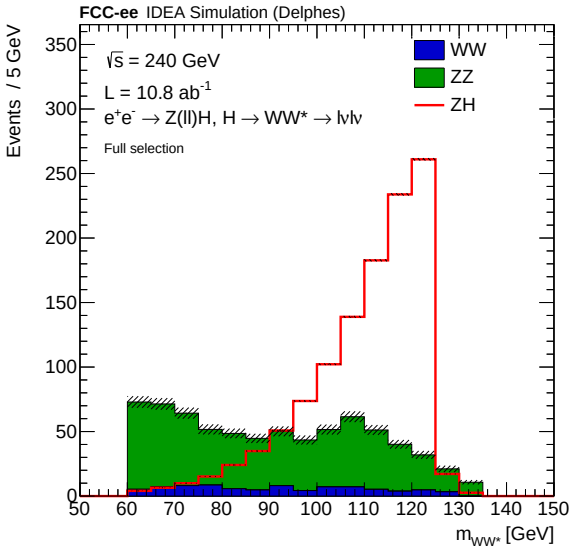
Figure 5: Expected signal and background yields after each successive selection requirement at the two centre-of-mass energies.



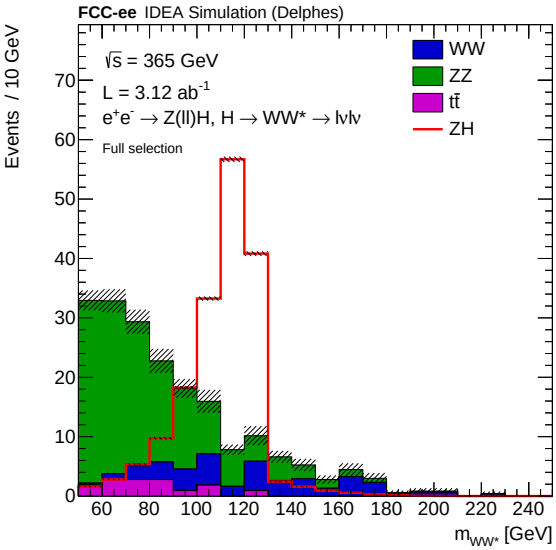
(a) m_{rec}, $\sqrt{s}$ = 240 GeV



(b) m_{rec}, $\sqrt{s}$ = 365 GeV



(c) m_{WW^*}, 240 GeV



(d) m_{WW^*}, 365 GeV

Figure 6: Higgs-boson mass reconstruction after the full event selection using the recoil mass (top) and the reconstructed WW^*-system mass (bottom), at 240 and 365 GeV.

8 Multivariate event classification

Following the kinematic selection, a Boosted Decision Tree (BDT) [24–26] is used to exploit correlations among the reconstructed observables and improve the separation of the Higgsstrahlung signal from the remaining backgrounds. Rather than applying a requirement on the classifier output, its continuous score is used as the discriminating variable in the binned maximum-likelihood fit described in Section 9. This retains the information in both signal-enriched and background-enriched regions and is expected to provide greater sensitivity than a cut-and-count approach.

Independent classifiers are trained at 240 and 365 GeV using dedicated signal and ZZ samples that are statistically independent of the samples used in the final analysis. Only ZZ, the dominant background after the kinematic selection, is included in the background training sample. The input variables are listed in Table 5; the complete sample sizes, training configuration and validation diagnostics are documented in Appendix F.

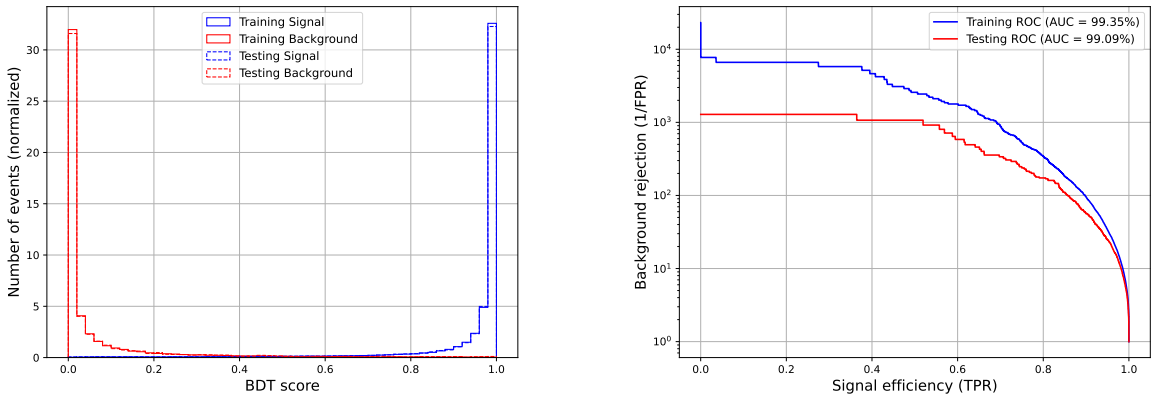
Table 5: Input variables used in the BDT classifiers at both centre-of-mass energies. The leptons $\ell_{1,\ldots,4}$ are ordered by momentum, while $\ell_{Z1,Z2}$ and $\ell_{W1,W2}$ denote the leading and subleading leptons assigned to the reconstructed Z- and WW^*-candidate systems, respectively.

Group	Variable(s)	Description
$Z \to \ell\ell$ system	$m_{\ell\ell}$	Invariant mass of the Z-candidate dilepton system
	$p_{\ell\ell}$, $\theta_{\ell\ell}$, $\phi_{\ell\ell}$	Momentum and direction of the Z candidate
	m_{rec}	Recoil mass against the Z candidate
	$\Delta R(\ell_{Z1}, \ell_{Z2})$	Angular separation of the Z-candidate leptons
	$p_{\ell_{Z1}}$, $p_{\ell_{Z2}}$	Momenta of the Z-candidate leptons
	$\theta_{\ell_{Z1}}$, $\theta_{\ell_{Z2}}$	Polar angles of the Z-candidate leptons
	$\phi_{\ell_{Z1}}$, $\phi_{\ell_{Z2}}$	Azimuthal angles of the Z-candidate leptons
WW^* system	m_{WW^*}	Invariant mass of the WW^* system
	p_{WW^*}, θ_{WW^*}, ϕ_{WW^*}	Momentum and direction of the WW^* system
	$m_{\ell_{W1}\ell_{W2}}$	Invariant mass of the W-candidate lepton pair
	$\Delta R(\ell_{W1}, \ell_{W2})$	Angular separation of the W-candidate leptons
	$\Delta\phi(\ell_{W1}, \ell_{W2})$	Azimuthal separation of the W-candidate leptons
	$p_{\ell_{W1}}$, $p_{\ell_{W2}}$	Momenta of the W-candidate leptons
	$\theta_{\ell_{W1}}$, $\theta_{\ell_{W2}}$	Polar angles of the W-candidate leptons
	$\phi_{\ell_{W1}}$, $\phi_{\ell_{W2}}$	Azimuthal angles of the W-candidate leptons
Event observables	n_e, n_μ	Numbers of electrons and muons
	p_{ℓ_1}, p_{ℓ_2}, p_{ℓ_3}, p_{ℓ_4}	Momenta of the four leptons
	$\Delta R(Z \to \ell\ell, WW^*)$	Angular separation of the reconstructed systems
	E_{miss}	Missing energy
	$\cos\theta_{\text{miss}}$	Polar direction of the missing momentum
	m_{miss}	Missing invariant mass

At both centre-of-mass energies, the observables with the greatest discriminating power are the reconstructed WW^*-system mass, m_{WW^*}, and the invariant mass of the W-candidate lepton pair, $m_{\ell_{W1}\ell_{W2}}$. The angular separation $\Delta R(\ell_{W1}, \ell_{W2})$ is also among the leading inputs at 365 GeV, consistent with the more collimated signal topology produced by the larger Higgs-boson boost discussed in Section 7.

Figure 7 shows the classifier response and receiver-operating-characteristic performance at 240 GeV. The agreement between the training and testing score distributions indicates no significant overtraining. The classifiers provide strong discrimination at both energy points, with Area Under the Curve (AUC) values of approximately 99%. The corresponding 365 GeV plots, together with the complete set of diagnostics for both energies, are given in Appendix F.

When evaluated on the full analysis samples, the classifier concentrates the ZZ background in the low-score region. The WW and $t\bar{t}$ backgrounds, which are not included in the training, tend to



(a) Training and testing score distributions

(b) Background rejection versus signal efficiency

Figure 7: Performance of the BDT-based classifier at $\sqrt{s} = 240$ GeV. The background rejection in the right panel is defined as the inverse of the background efficiency.

populate higher-score bins; their contributions are included as background templates in the final fit. Comparing fits with only the ZZ background and with all background processes gives very similar expected precision, indicating that their absence from the training does not degrade the final sensitivity.

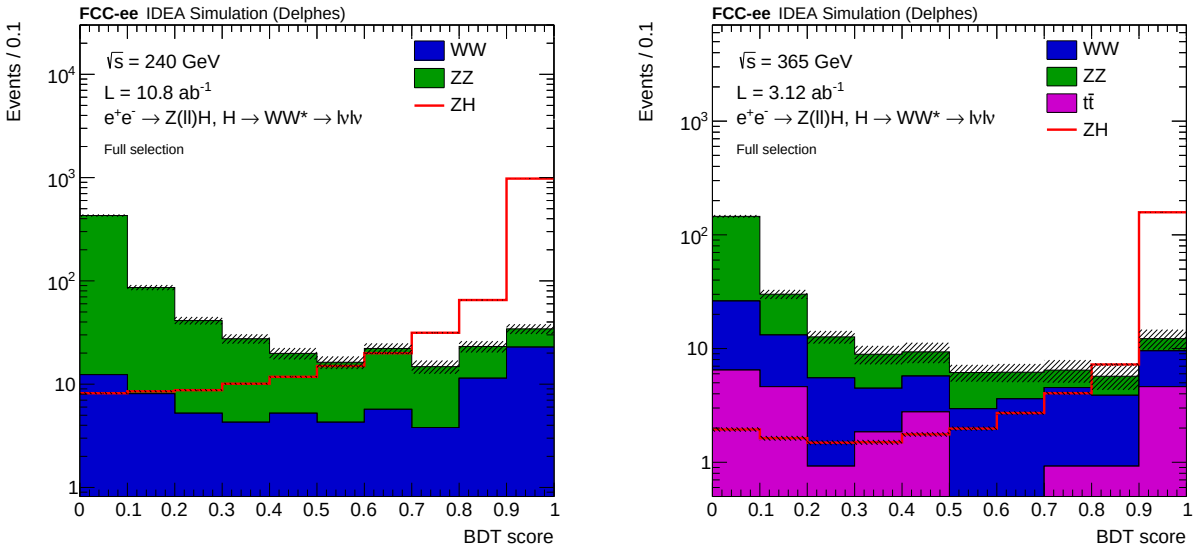
9 Results

The trained BDT models are evaluated on the full analysis samples, yielding BDT output score distributions for both the 240 GeV and 365 GeV datasets, as shown in Figure 8. These score distributions are used as the discriminating variables in a binned maximum-likelihood fit implemented with CMS Combine (version 9.2.1) to extract the expected precision on the signal strength, μ. The signal strength is defined relative to the SM expectation for $\sigma_{ZH} \times \mathcal{B}(H \to WW^*)$. In the likelihood, μ scales the complete simulated signal template, including the residual ZZ-fusion-plus-interference contribution in the electron channel. The expected precision is evaluated using an Asimov dataset assuming $\mu = 1$ and extracted from the covariance matrix of the maximum-likelihood fit. With the leptonic branching fractions and signal efficiency treated as fixed inputs, the relative uncertainty $\Delta\mu/\mu$ directly represents the expected precision on the cross section times branching fraction.

In this fit, statistical uncertainties arising from the finite MC sample sizes are incorporated using Combine's `autoMCStats` procedure, together with a 1% systematic uncertainty on the total background normalization. The latter is modelled using a log-normal nuisance parameter, correlated across the BDT-score bins but uncorrelated between the two centre-of-mass energies. The impact of these uncertainties on the final precision is found to be negligible for both datasets, indicating that the measurements are statistically limited.

For the $\sqrt{s} = 240$ GeV analysis, the expected precision extracted from the fit is 3.09%, while for the $\sqrt{s} = 365$ GeV analysis, the expected precision is 7.33%. These results are compared with the ultimate precision introduced in Section 3 and summarized in Table 6. At 240 GeV, the ultimate precision is 2.60%, such that the expected precision corresponds to a relative degradation of 19%. At 365 GeV, the corresponding ultimate precision is 6.20%, resulting in a degradation of 18%.

The weaker absolute precision at 365 GeV reflects the smaller signal sample: the integrated luminosity is 3.12 ab^{-1} rather than 10.8 ab^{-1}, and the ZH production cross section is approximately 125 fb rather than 201 fb. The degradation relative to the ideal statistical limit is partially driven



(a) $\sqrt{s}$ = 240 GeV (b) $\sqrt{s}$ = 365 GeV

Figure 8: BDT output score distributions obtained by evaluating the trained classifiers on the full analysis samples at the two centre-of-mass energies. The vertical axes are shown on a logarithmic scale.

Table 6: Expected relative precision on $\sigma_{ZH} \times \mathcal{B}(H \to WW^*)$ compared with the ultimate statistical limit, defined assuming 100% signal acceptance and no background contribution. The degradation is quoted relative to the ultimate precision.

$\sqrt{s}$ [GeV]	Expected precision	Ultimate precision	Relative degradation
240	3.09%	2.60%	19%
365	7.33%	6.20%	18%
Combined	2.90%	2.40%	21%

by the strategy used to suppress the ZZ-fusion-plus-interference contribution, which becomes non-negligible at this higher centre-of-mass energy. At 365 GeV, the recoil-mass-only pairing scheme adopted to avoid artificially reconstructing the nonresonant electron-channel contribution near the Z-boson mass decreases the pairing efficiency for genuine ZH events. In addition, the reconstructed Z-candidate dilepton invariant-mass distribution is broader than at 240 GeV, including in the muon channel, which contains only the ZH contribution. The subsequent requirement on $m_{\ell\ell}$, used to strongly suppress the ZZ-fusion-plus-interference component in the electron channel, reduces the ZH signal acceptance and hence contributes to the reduced measurement precision at 365 GeV.

The ZH signal and ZZ-fusion-plus-interference components could be further separated by training a multiclass classifier with dedicated VBF signal samples, accounting for both contributions simultaneously in the maximum-likelihood fit. Furthermore, the analysis at 365 GeV could benefit from the implementation of a b-jet veto, which would provide additional suppression against the remaining backgrounds, such as $t\bar{t}$ production.

Assuming the production cross section uncertainties for both centre-of-mass energies are negligible, the two energy points can be combined in a simultaneous fit. The combined likelihood is formed from the statistically independent 240 and 365 GeV BDT-score distributions, with a

common signal-strength parameter μ controlling the signal contribution in both datasets. The simultaneous fit yields an expected relative precision of 2.90%. The corresponding ultimate statistical precision, obtained by combining the ideal statistical limits of the two datasets, is approximately 2.40%, resulting in a relative degradation of 21%. The combination is dominated by the 240 GeV dataset, as it contains a substantially larger selected signal sample and has a more favorable signal-to-background ratio. The 365 GeV dataset adds a modest amount of statistical information, improving the expected combined precision by approximately 6% relative to the 240 GeV result.

When combined with the existing $\sqrt{s} = 240$ GeV $H \to WW^*$ projections summarized in Section 1.3, the corresponding result presented here provides an additional independent contribution to the overall sensitivity. Assuming the measurements are statistically independent and neglecting correlations between their uncertainties, its inclusion improves the expected combined precision by approximately 3.4%, yielding a precision of about 0.8% on $\sigma_{ZH} \times \mathcal{B}(H \to WW^*)$.

10 Conclusions

In this note, a detailed feasibility study for the measurement of the $e^+e^- \to ZH$ production cross section times the $H \to WW^*$ branching fraction in the fully leptonic final state was presented. The analysis evaluated the expected performance at the FCC-ee, assuming integrated luminosities of 10.8 ab^{-1} at $\sqrt{s} = 240$ GeV and 3.12 ab^{-1} at $\sqrt{s} = 365$ GeV, using a parameterized simulation of the IDEA detector concept. BDT-based event classification was used to increase the separation between the signal and the dominant backgrounds, most notably the irreducible ZZ process. The expected measurement precision was then extracted by performing a binned maximum-likelihood fit to the final BDT output score distribution.

At $\sqrt{s} = 240$ GeV, the expected relative precision on $\sigma_{ZH} \times \mathcal{B}(H \to WW^*)$ is evaluated to be 3.09%. This is 19% larger than the ideal statistical limit of 2.60% for this channel. When combined with the existing 240 GeV $H \to WW^*$ projections discussed in Section 1.3, this fully leptonic channel improves the expected combined precision by approximately 3.4%, yielding an overall precision of about 0.8%. On the other hand, for the $\sqrt{s} = 365$ GeV dataset, the expected relative precision is determined to be 7.33%, which is 18% larger than the ideal statistical limit of 6.20%. The smaller signal yield and the loss of ZH acceptance – associated with suppressing the ZZ-fusion-plus-interference contribution – could explain the lower sensitivity for the 365 GeV dataset. Finally, the simultaneous fit to the statistically independent 240 and 365 GeV datasets yields an expected combined precision of 2.90% on $\sigma_{ZH} \times \mathcal{B}(H \to WW^*)$. The combination is dominated by the 240 GeV dataset and therefore improves only modestly upon its standalone precision. This result highlights the exceptional capability of the FCC-ee to measure the $H \to WW^*$ decay mode in the fully leptonic channel, providing an important input for the global Higgs coupling fit programme.

References

[1] M. Benedikt et al. Future Circular Collider Feasibility Study Report: Volume 1, Physics, Experiments, Detectors. *Eur. Phys. J. C*, 85(12):1468, 2025. arXiv:2505.00272, doi:10.1140/epjc/s10052-025-15077-x.

[2] M. Benedikt et al. Future Circular Collider Feasibility Study Report: Volume 2, Accelerators, Technical Infrastructure and Safety. *Eur. Phys. J. ST*, 234(19):5713–6197, 2025. arXiv:2505.00274, doi:10.1140/epjs/s11734-025-01967-4.

[3] M. Benedikt et al. Future Circular Collider Feasibility Study Report. *Eur. Phys. J. ST*, 234(17):5113–5383, 2025. [Erratum: Eur.Phys.J.ST 234, 33–44 (2025)]. arXiv:2505.00273, doi:10.1140/epjs/s11734-025-01958-5.

[4] S. Navas et al. Review of Particle Physics. *Phys. Rev. D*, 110(3):030001, 2024. doi:10.1103/PhysRevD.110.030001.

[5] Ang Li, Jan Eysermans, Gregorio Bernardi, Kevin Dewyspelaere, Michele Selvaggi, and Christoph Paus. Model-independent ZH production cross section at FCC-ee. 12 2025. arXiv:2512.21290.

[6] Andrea Del Vecchio, Jan Eysermans, Loukas Gouskos, George Iakovidis, Alexis Maloizel, Giovanni Marchiori, and Michele Selvaggi. Precision measurements of Higgs hadronic decay modes at the FCC-ee. *JHEP*, 04:181, 2026. arXiv:2511.23149, doi:10.1007/JHEP04(2026)181.

[7] Georges Aad et al. Measurements of Higgs boson production by gluon-gluon fusion and vector-boson fusion using $H \to WW^* \to e\nu\mu\nu$ decays in pp collisions at $\sqrt{s} = 13$ TeV with the ATLAS detector. *Phys. Rev. D*, 108:032005, 2023. arXiv:2207.00338, doi:10.1103/PhysRevD.108.032005.

[8] Armen Tumasyan et al. Measurements of the Higgs boson production cross section and couplings in the W boson pair decay channel in proton-proton collisions at $\sqrt{s} = 13$ TeV. *Eur. Phys. J. C*, 83(7):667, 2023. arXiv:2206.09466, doi:10.1140/epjc/s10052-023-11632-6.

[9] ATLAS Collaboration. Measurements of the production cross-sections of a higgs boson in association with a vector boson and decaying into WW^* with the ATLAS detector at $\sqrt{s} = 13$ TeV. *JHEP*, 08:034, 2025. arXiv:2503.19420, doi:10.1007/JHEP08(2025)034.

[10] D. de Florian et al. Handbook of LHC Higgs Cross Sections: 4. Deciphering the Nature of the Higgs Sector. *CERN Yellow Rep. Monogr.*, 2:1–869, 2017. arXiv:1610.07922, doi:10.23731/CYRM-2017-002.

[11] CMS Collaboration. Measurement of WWZ and ZH Production Cross Sections at $\sqrt{s} = 13$ and 13.6 TeV. *Phys. Rev. Lett.*, 135(9):091802, 2025. arXiv:2505.20483, doi:10.1103/6z3d-zjw4.

[12] Mila Pandurović. Physics Potential for the Measurement of $\sigma(HZ) \times BR(H \to WW^*)$ at the 250 GeV ILC. In *International Workshop on Future Linear Colliders*, 2 2019. arXiv:1902.08032.

[13] Xiaotian Ma, Zuofei Wu, Jinfei Wu, Yanping Huang, Gang Li, Manqi Ruan, Fábio L. Alves, Shan Jin, and Ligang Shao. Measurements of decay branching fractions of the Higgs boson to hadronic final states at the CEPC*. *Chin. Phys. C*, 49(5):053001, 2025. arXiv:2410.04465, doi:10.1088/1674-1137/adacc5.

[14] Jan Eysermans, Haydee Hernandez Arellano, Felipe de Jesús Martínez Tapia, and Maria Isabel Pedraza Morales. *Measurement of the Higgs boson decay in $Z(ll)H, H \to WW^*$ at the FCC-ee at $\sqrt{s} = 240$ GeV*, March 2025. doi:10.17181/1d9a2-qqm10.

[15] Jan Eysermans, Michele Selvaggi, Aman Mukeshbhai Desai, and Mila Pandurovic. *hww* and *hzz* in the fully hadronic final states at the fcc-ee, March 2025. doi:10.17181/jxx9k-b9z97.

[16] Michele Selvaggi, Jan Eysermans, and Alain Blondel. Prospects in electroweak, higgs and top physics at fcc, March 2025. doi:10.17181/n2emg-43f06.

[17] M. Abbrescia et al. The IDEA detector concept for FCC-ee. 2 2025. arXiv:2502.21223.

[18] J. de Favereau, C. Delaere, P. Demin, A. Giammanco, V. Lemaître, A. Mertens, and M. Selvaggi. DELPHES 3: a modular framework for fast simulation of a generic collider experiment. *JHEP*, 02:057, 2014. arXiv:1307.6346, doi:10.1007/JHEP02(2014)057.

[19] HEP-FCC. IDEA detector card for Delphes, winter2023 configuration, 2023. FCC configuration repository, accessed 2 August 2026. URL: https://github.com/HEP-FCC/FCC-config/blob/winter2023/FCCee/Delphes/card_IDEA.tcl.

[20] Wolfgang Kilian, Thorsten Ohl, and Jurgen Reuter. WHIZARD: Simulating Multi-Particle Processes at LHC and ILC. *Eur. Phys. J. C*, 71:1742, 2011. arXiv:0708.4233, doi:10.1140/epjc/s10052-011-1742-y.

[21] Torbjorn Sjostrand, Stephen Mrenna, and Peter Z. Skands. PYTHIA 6.4 Physics and Manual. *JHEP*, 05:026, 2006. arXiv:hep-ph/0603175, doi:10.1088/1126-6708/2006/05/026.

[22] Torbjörn Sjöstrand, Stefan Ask, Jesper R. Christiansen, Richard Corke, Nishita Desai, Philip Ilten, Stephen Mrenna, Stefan Prestel, Christine O. Rasmussen, and Peter Z. Skands. An introduction to PYTHIA 8.2. *Comput. Phys. Commun.*, 191:159–177, 2015. arXiv:1410.3012, doi:10.1016/j.cpc.2015.01.024.

[23] Jan Eysermans, Ang Li, Gregorio Bernardi, Christoph Paus, Emmanuel Perez, and Michele Selvaggi. Toward a Measurement of the Higgs Boson Mass with Natural-Width Precision at FCC-ee. 8 2026. arXiv:2608.12071.

[24] Leo Breiman, Jerome Friedman, R. A. Olshen, and Charles J. Stone. *Classification and Regression Trees*. Chapman and Hall/CRC, 10 2017. doi:10.1201/9781315139470.

[25] Yoav Freund and Robert E. Schapire. Experiments with a new boosting algorithm. In *International Conference on Machine Learning*, 1996. URL: https://api.semanticscholar.org/CorpusID:1836349.

[26] Yoav Freund and Robert E. Schapire. A Decision-Theoretic Generalization of On-Line Learning and an Application to Boosting. *J. Comput. Syst. Sci.*, 55(1):119–139, 1997. doi:10.1006/jcss.1997.1504.

[27] Tianqi Chen and Carlos Guestrin. Xgboost: A scalable tree boosting system. In *Proceedings of the 22nd acm sigkdd international conference on knowledge discovery and data mining*, pages 785–794, 2016. doi:10.1145/2939672.2939785.

A Monte Carlo sample details

This appendix documents the simulated samples used in the analysis. The sample identifiers, production cross sections, and numbers of processed events are summarized in Table 7.

Table 7: Signal and background MC samples from the *winter2023* campaign and their cross sections and numbers of simulated (processed) events at 240 and 365 GeV. The 240 GeV signal cross sections correspond to samples generated in the fully leptonic $H \to WW^*$ final state, including $W \to \tau\nu$ decays, which are not considered in this analysis, whereas the 365 GeV signal cross sections are inclusive in the W-boson decays. Sample identifiers beginning with `wzp6` denote samples generated with WHIZARD interfaced to PYTHIA 6, while those beginning with `p8` denote samples generated with PYTHIA 8.

		$\sqrt{s}$ = 240 GeV		$\sqrt{s}$ = 365 GeV	
Process	Sample	σ [pb]	N_{events}	σ [pb]	N_{events}
Signal samples					
$e^+e^- \to e^+e^-H, H \to WW^*$	`wzp6_ee_eeH_HWW`		—	0.00159	1,100,000
$e^+e^- \to \mu^+\mu^-H, H \to WW^*$	`wzp6_ee_mumuH_HWW`		—	0.0009007	1,100,000
$e^+e^- \to e^+e^-H, H \to WW^* \to \ell\nu\ell\nu$	`wzp6_ee_eeH_HWW_llnunu`	0.0001633	500,000		—
$e^+e^- \to \mu^+\mu^-H, H \to WW^* \to \ell\nu\ell\nu$	`wzp6_ee_mumuH_HWW_llnunu`	0.0001543	500,000		—
Background samples					
$e^+e^- \to ZZ$	`p8_ee_ZZ`	1.35899	56,162,093	0.6428	61,470,944
$e^+e^- \to W^+W^-$	`p8_ee_WW`	16.4385	373,375,386	10.7165	101,754,213
$e^+e^- \to t\bar{t}$	`p8_ee_tt`		—	0.800	2,700,000
$e^+e^- \to e^+e^-$	`wzp6_ee_ee_Mee_30_150`	8.305	85,400,000	1.53	3,000,000
$e^+e^- \to \mu^+\mu^-$	`wzp6_ee_mumu`	5.288	53,400,000	2.287	6,600,000

A.1 Event generators and signal filtering

The signal and non-Higgs samples with purely leptonic final states are generated with WHIZARD for the hard-scattering matrix element, interfaced to PYTHIA 6 for decays, parton showering, fragmentation, and hadronization. The inclusive diboson and top-quark background samples are generated with PYTHIA 8 for the complete generation chain.

At 240 GeV, the signal samples are generated directly in the fully leptonic $H \to WW^* \to \ell\nu\ell\nu$ final state, including direct electron, muon, and tau decays of the W bosons. The generated electron- and muon-Z-channel cross sections are 0.1633 and 0.1543 fb. A generator-level filter removes the $W \to \tau\nu$ decays. Its efficiency is approximately 44%, leaving about 220,000 events per channel for the analysis.

At 365 GeV, inclusive $H \to WW^*$ samples are used and a generator-level filter selects the $\ell\nu\ell\nu$ final state. Their inclusive cross sections are 1.59 fb and 0.9007 fb for the electron and muon channels, respectively. A total of 1.1×10^6 events is simulated for each process; the filter efficiency is approximately 4.6%, leaving about 50,600 events per channel for the analysis.

A.2 Background topologies

This subsection describes the decay topologies through which the background processes can satisfy the four-lepton selection. Representative tree-level production diagrams are shown in Figure 9.

The irreducible ZZ background is dominated by $ZZ \to \ell^+\ell^-\tau^+\tau^-$ events in which both tau leptons decay leptonically. The WW process normally contains only two prompt charged leptons

when both W bosons decay leptonically. It can enter the four-lepton selection when an initial- or final-state radiation photon converts into an additional e^+e^- pair, for example

$$W^+W^- \to (\ell^+\nu)(\ell^-\bar{\nu}), \qquad \gamma \to e^+e^-.$$

The inclusive WW sample also contains semileptonic and fully hadronic W-boson decays. Representative decay chains capable of supplying four reconstructed leptons are

$$\begin{aligned} &W^+W^- \to (\ell^+\nu)(\bar{c}s), && \bar{c} \to \bar{s}\ell^-\bar{\nu}, && \gamma \to e^+e^-, \\ &W^+W^- \to (c\bar{s})(\bar{c}s), && c \to s\ell^+\nu, \quad \bar{c} \to \bar{s}\ell^-\bar{\nu}, && \gamma \to e^+e^-, \end{aligned}$$

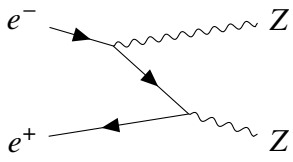
where charge-conjugate decay chains are implied. Other combinations of semileptonic hadron decays and converted radiated photons can contribute in the inclusive sample. Indeed, after the analysis selection, the yield obtained from a dedicated fully leptonic WW sample is approximately a factor of two smaller than that obtained from the inclusive WW sample, demonstrating that the surviving background is not exclusively due to fully leptonic WW decays accompanied by a converted photon. Because these processes have large inclusive cross sections but very small selection efficiencies, samples containing tens to hundreds of millions of events are processed.

At 365 GeV, each top quark decays as $t \to Wb$. If both W bosons decay leptonically and the b-quarks subsequently undergo semileptonic decays as $b \to c\ell\nu$, the event contains four charged leptons and several neutrinos. At quark level, a representative decay chain is

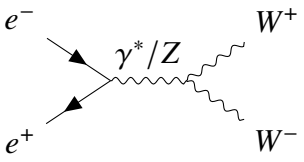
$$t\bar{t} \to bW^+\bar{b}W^- \to (c\ell^-\bar{\nu})(\ell^+\nu)(\bar{c}\ell^+\nu)(\ell^-\bar{\nu}).$$

Another contribution arises from the ordinary dileptonic $t\bar{t}$ decay when a radiated photon converts into an additional lepton pair.

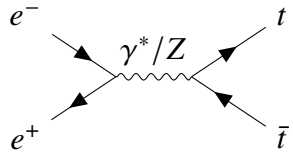
The inclusive two-lepton samples are included to test backgrounds with no genuine missing momentum. The Bhabha sample is generated with $30 < M_{ee} < 150$ GeV at matrix-element level to regulate the low-mass divergence. Neither the electron nor muon two-lepton sample survives the four-lepton requirement.



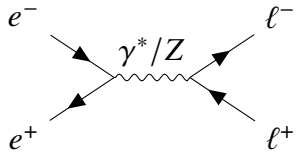
(a) $e^+e^- \to ZZ$



(b) $e^+e^- \to W^+W^-$



(c) $e^+e^- \to t\bar{t}$

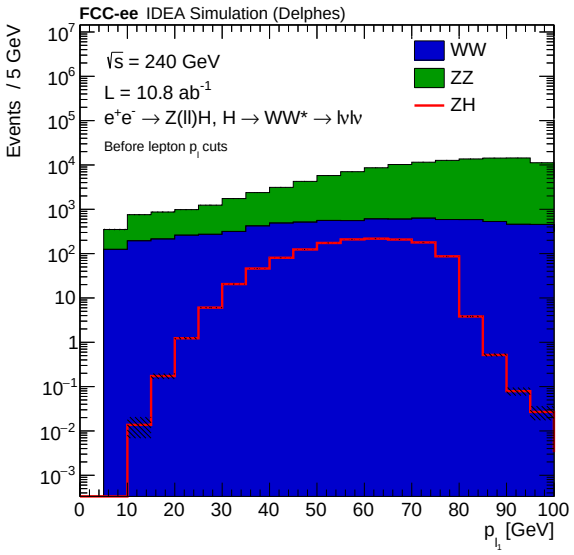


(d) $e^+e^- \to \ell^+\ell^-$

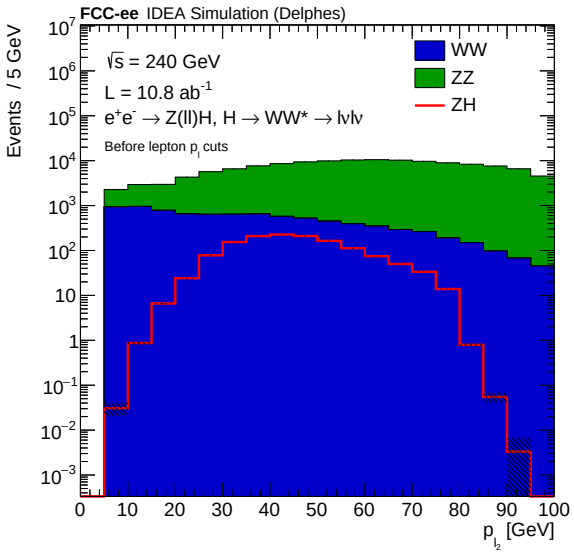
Figure 9: Representative tree-level diagrams of the backgrounds considered in the $H \to WW^* \to \ell\nu\ell\nu$ study: (a) $e^+e^- \to ZZ$ via t-channel electron exchange; (b) $e^+e^- \to W^+W^-$ via an s-channel γ^*/Z propagator; (c) $e^+e^- \to t\bar{t}$ via an s-channel γ^*/Z propagator; and (d) charged-lepton-pair production through $e^+e^- \to \gamma^*/Z \to \ell^+\ell^-$. For $\ell = e$, Bhabha scattering also receives a t-channel contribution, which is not shown.

B Additional preselection distributions

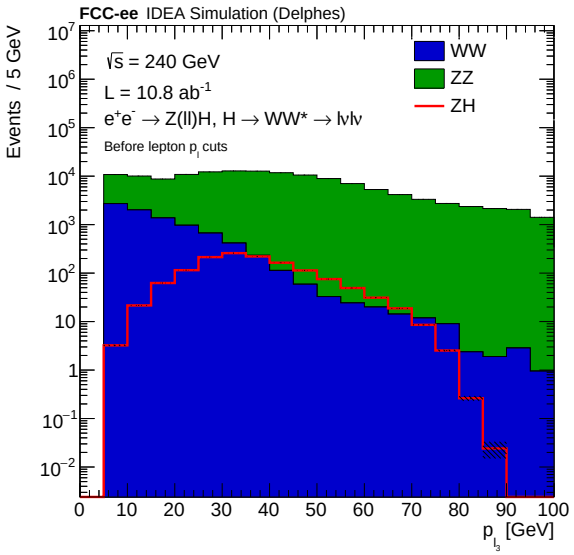
This appendix collects the ordered-lepton momentum distributions in Figures 10 and 11, which are used to define the preselection requirements described in Section 4, and the complete set of lepton-isolation distributions at $\sqrt{s} = 365$ GeV in Figure 12.



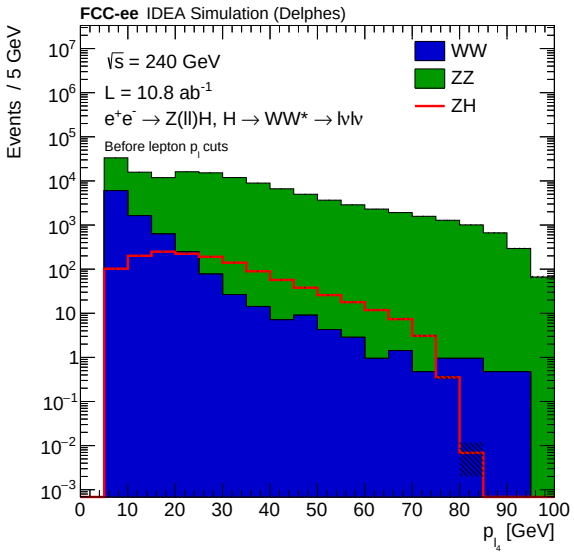
(a) Leading lepton, ℓ_1



(b) Subleading lepton, ℓ_2

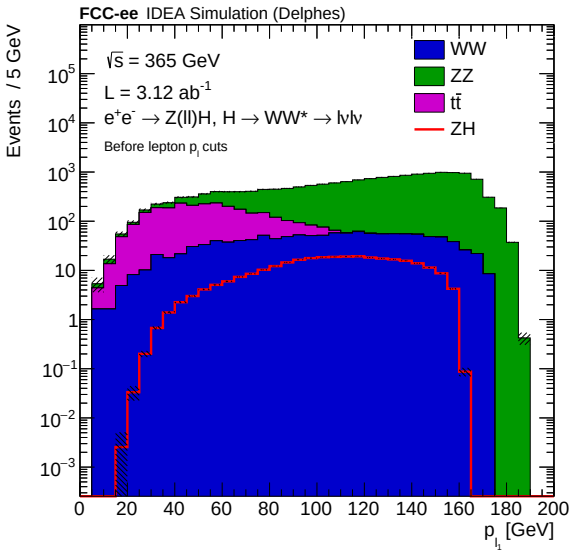


(c) Third lepton, ℓ_3

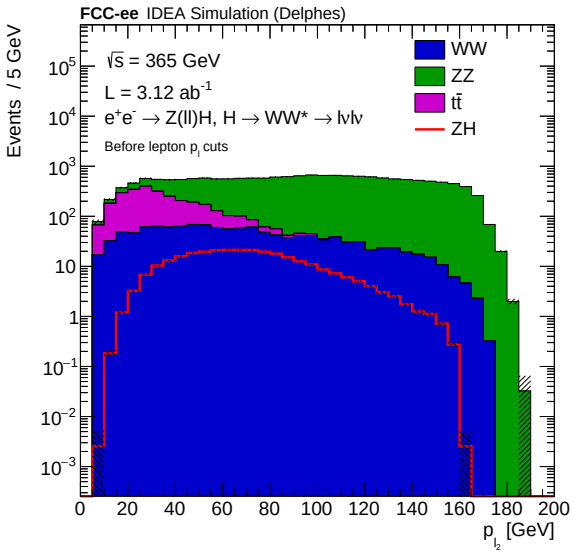


(d) Fourth lepton, ℓ_4

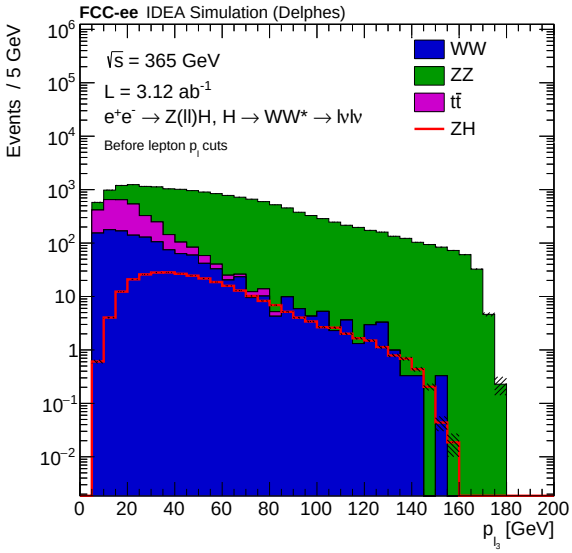
Figure 10: Momentum distributions of the four reconstructed leptons, ordered from highest to lowest momentum, at $\sqrt{s} = 240$ GeV after the four-lepton, opposite-sign-pair, and same-flavour-pair requirements and before the lepton-momentum selection.



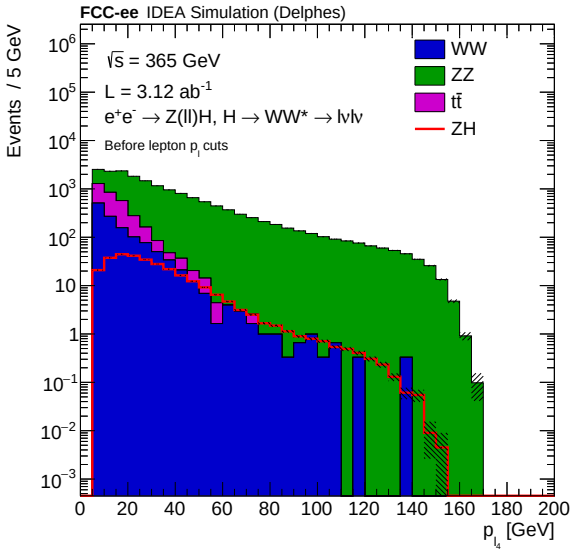
(a) Leading lepton, ℓ_1



(b) Subleading lepton, ℓ_2

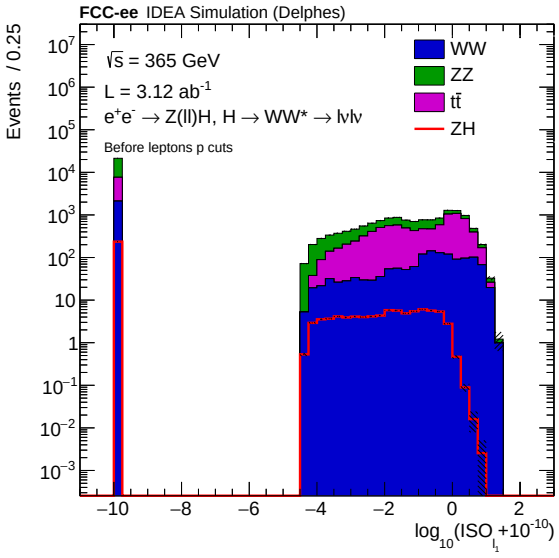


(c) Third lepton, ℓ_3

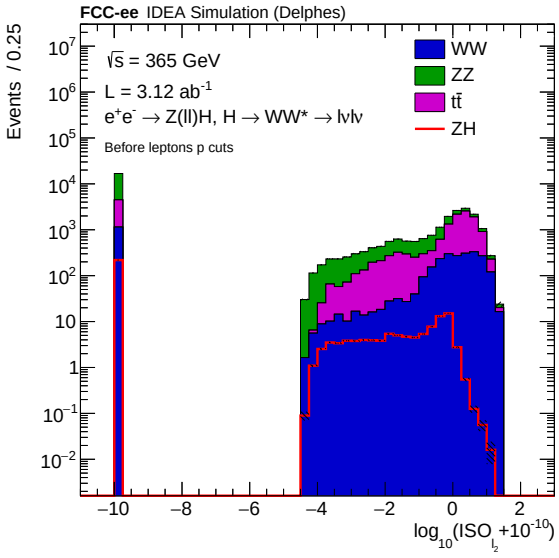


(d) Fourth lepton, ℓ_4

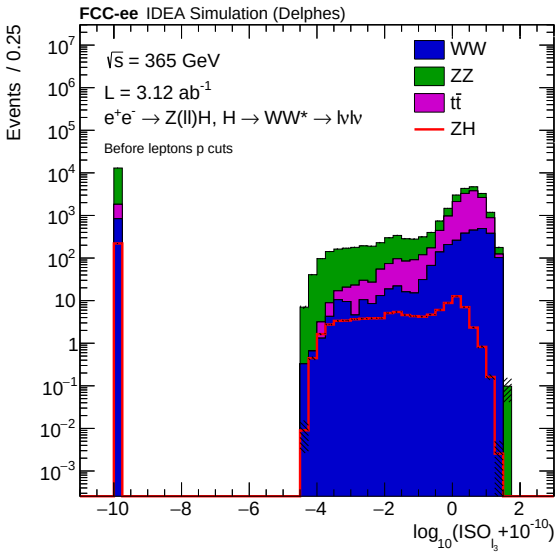
Figure 11: Momentum distributions of the four reconstructed leptons, ordered from highest to lowest momentum, at $\sqrt{s} = 365$ GeV after the four-lepton, opposite-sign-pair, and same-flavour-pair requirements and before the lepton-momentum selection.



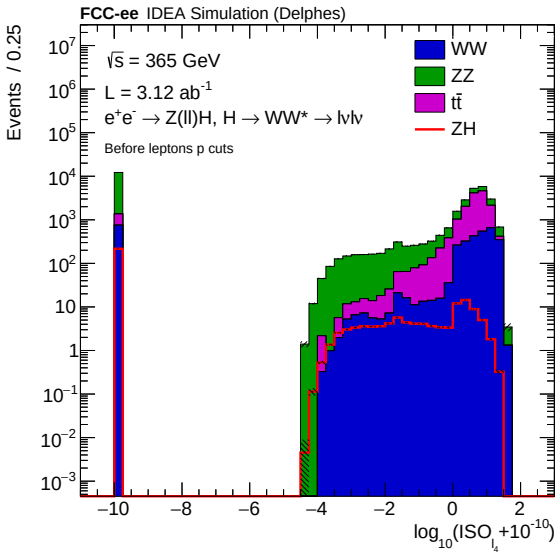
(a) Leading lepton, ℓ_1



(b) Subleading lepton, ℓ_2



(c) Third lepton, ℓ_3



(d) Fourth lepton, ℓ_4

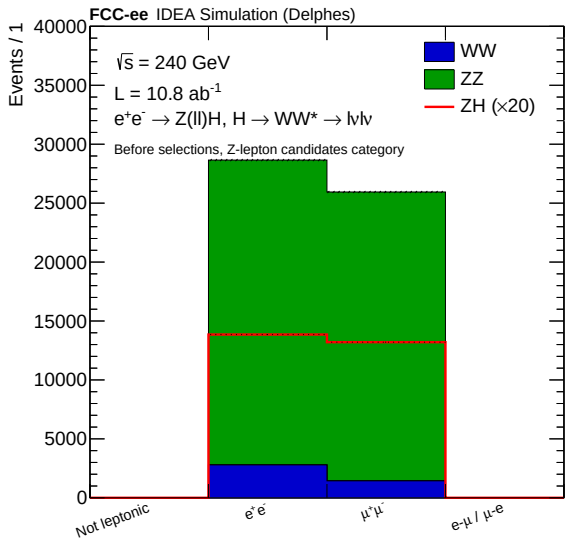
Figure 12: Distributions of the logarithm of the isolation for the four reconstructed leptons, $\log_{10}(\mathrm{ISO}_\ell)$, ordered from highest to lowest momentum, at $\sqrt{s}$ = 365 GeV. All preselection requirements other than the lepton isolation and momentum requirements are applied. A value of 10^{-10} is added to the isolation observable to represent zero-isolation entries consistently on the logarithmic scale.

C Leptonic category composition

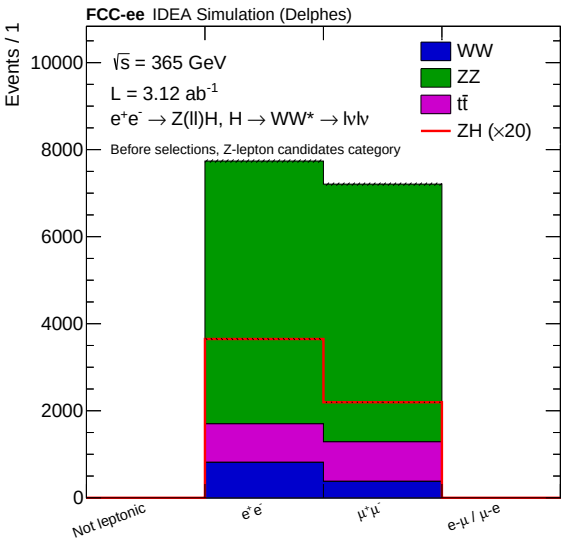
Figure 13 shows the flavour composition of the reconstructed Z- and WW^*-candidate lepton pairs before the optimized event selection.

For the reconstructed Z candidate at 240 GeV, the signal follows the expectation from SM lepton universality: events are evenly divided between the ee and $\mu\mu$ channels, with no contribution to the mixed-flavour ($e^{\pm}\mu^{\mp}$) category. At 365 GeV, however, the signal exhibits a clear excess in the ee bin before the optimized selection. This asymmetry arises because the inclusive electron-channel signal sample contains the additional ZZ-fusion-plus-interference contribution, whereas the muon channel contains only Higgsstrahlung. The Z-mass requirement strongly suppresses this nonresonant component, leaving similar selected signal yields in the ee and $\mu\mu$ bins, as shown in Appendix D, Figure 15. The backgrounds also exhibit an excess in the ee assignment; one possible source is the conversion of photons from initial- or final-state radiation into additional reconstructed electron pairs.

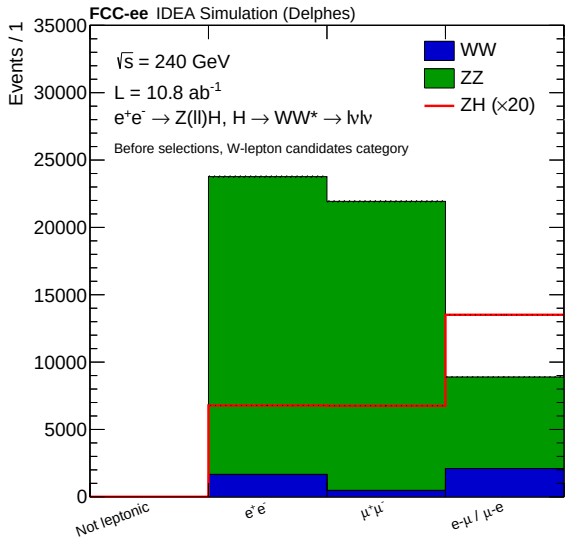
The signal distribution for the reconstructed WW^* system at both centre-of-mass energies approximately follows the expected 1 : 1 : 2 ratio between the ee, $\mu\mu$ and mixed-flavour categories, since the mixed-flavour bin combines both the $e\mu$ and μe permutations. The WW background shows a similar electron-heavy asymmetry. The dominant ZZ background populates both the same- and mixed-flavour W-candidate categories. A major contribution is expected from $ZZ \to \ell^+\ell^-\tau^+\tau^-$ events in which both tau leptons decay leptonically. These decays can populate the ee, $\mu\mu$, and mixed-flavour categories and provide genuine missing momentum from the neutrinos. Their simple decay-level flavour proportions are not preserved in the reconstructed distribution because of lepton pairing, the event selection, and the presence of other ZZ decay topologies. In particular, an additional contribution to the ee category can arise from $ZZ \to \ell^+\ell^- q\bar{q}$ events accompanied by a radiated photon that converts into an e^+e^- pair.



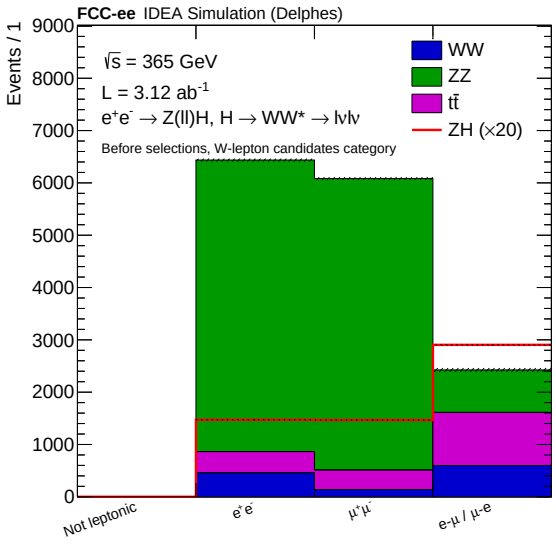
(a) Z-candidate leptons at $\sqrt{s}$ = 240 GeV



(b) Z-candidate leptons at $\sqrt{s}$ = 365 GeV



(c) WW^*-candidate leptons at $\sqrt{s}$ = 240 GeV



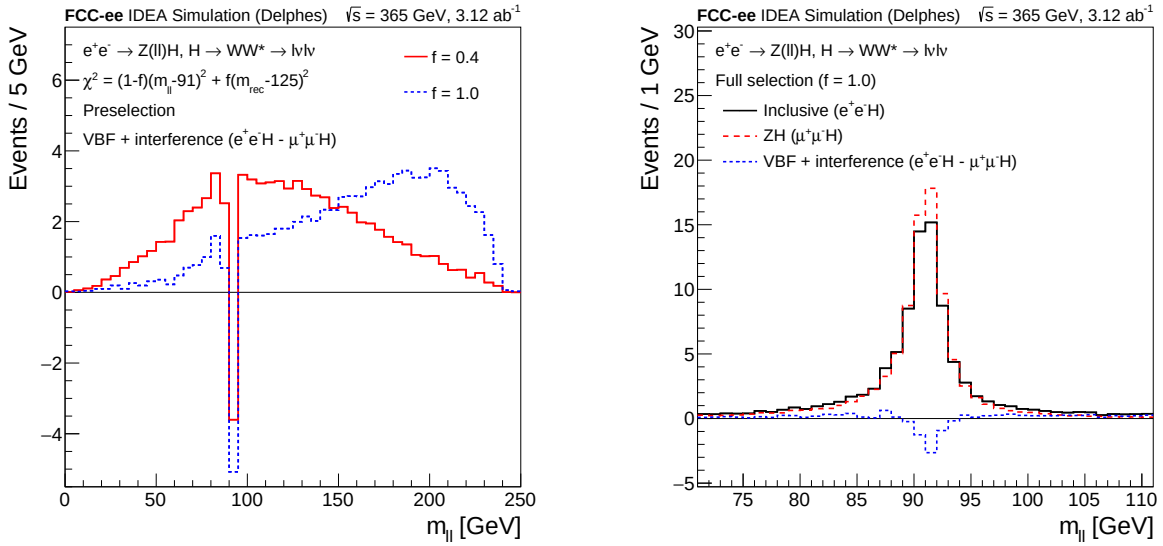
(d) WW^*-candidate leptons at $\sqrt{s}$ = 365 GeV

Figure 13: Lepton-flavour categories of the reconstructed Z- (top) and WW^*-candidate pairs (bottom) at $\sqrt{s}$ = 240 and 365 GeV before the optimized event selections. For visibility, the total signal yield is scaled by a factor of 20.

D Signal decomposition and additional ZZ-fusion studies

D.1 Effect of the lepton-pairing metric

The reconstructed dilepton-mass distributions obtained with $f = 0.4$ and $f = 1.0$ are shown in Figures 4a and 4b, respectively, for the ZH and ZZ-fusion-plus-interference components. The resulting migration of the isolated ZZ-fusion-plus-interference component is compared between these two values of f in Figure 14a, and the distribution with final event selection is shown in Figure 14b.



(a) Direct comparison of $f = 0.4$ and $f = 1.0$

(b) Final selection with $f = 1.0$

Figure 14: Reconstructed dilepton invariant-mass distributions used to study the ZZ-fusion contribution at $\sqrt{s} = 365$ GeV. (a) The ZZ-fusion-plus-interference component is compared between the two pairing schemes. (b) The final selection with $f = 1.0$ is shown for the inclusive electron channel, the muon-channel ZH proxy, and their difference, corresponding to the ZZ-fusion-plus-interference component.

The same suppression is visible in the flavour composition of the reconstructed Z candidate. Before the optimized selection, the signal ee yield in Figure 13b exceeds the $\mu\mu$ yield because the electron sample contains Higgsstrahlung, ZZ-fusion, and their interference, while the muon sample contains only Higgsstrahlung. After the full selection, the ee and $\mu\mu$ signal yields are similar, as shown in Figure 15. This is consistent with the strong suppression of the additional nonresonant electron-channel contribution provided by the Z-mass requirement.

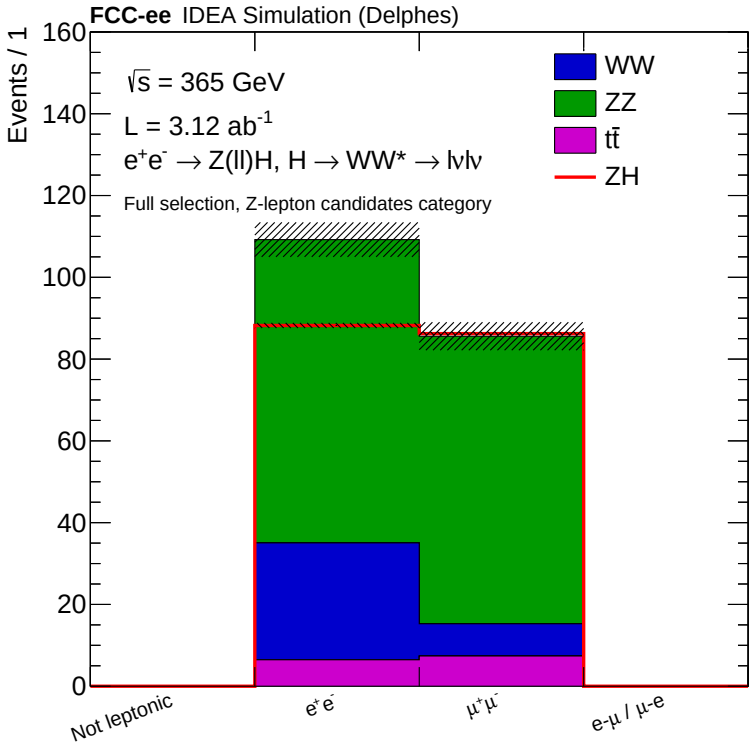


Figure 15: Flavour composition of the reconstructed Z-candidate leptons at $\sqrt{s} = 365$ GeV after the full event selection. The similar signal yields in the ee and $\mu\mu$ bins show the suppression of the additional ZZ-fusion-plus-interference contribution present in the inclusive electron sample.

D.2 Additional VBF suppression variables

As the primary goal of this analysis is to study the Higgsstrahlung process, suppression of the VBF component is required. Several topological and kinematic variables are examined as potential VBF suppressors, including the squared momentum transfers of the incident electron and positron (q_1^2 and q_2^2), the acollinearity between the Z-candidate leptons, the transverse momenta of the individual $Z \to \ell\ell$ leptons ($p_{\mathrm{T}}^{\ell_{Z1}}$ and $p_{\mathrm{T}}^{\ell_{Z2}}$), and the dilepton transverse momentum ($p_{\mathrm{T}}^{\ell\ell}$). The *momentum transfers* are defined as

$$q_1 \equiv p_{e^-}^{\mathrm{in}} - p_{e^-}^{\mathrm{out}} \quad \text{and} \quad q_2 \equiv p_{e^+}^{\mathrm{in}} - p_{e^+}^{\mathrm{out}}, \tag{5}$$

where the incoming four-momenta are fixed by the beam configuration and the outgoing momenta are those of the reconstructed electron and positron assigned to the Z candidate. Consequently, q_1^2 and q_2^2 are the virtualities, defined as the invariant four-momenta squared, carried by the two t-channel vector boson propagators in the ZZ-fusion process. The *acollinearity* is the deviation from a back-to-back configuration of the two Z-candidate leptons:

$$\alpha_{\mathrm{acol}} \equiv \pi - \theta_{12}, \tag{6}$$

where θ_{12} is the opening angle between them. It vanishes when the two leptons are exactly back-to-back and increases as their opening angle decreases.

These variables are motivated by the distinct phenomenological nature of the t-channel VBF process compared to resonant s-channel ZH production. Because the initial-state electron and positron in VBF events scatter at very shallow angles, their trajectories are very close to the beam axis. Consequently, the difference in their initial and final four-momenta is minimal, causing the

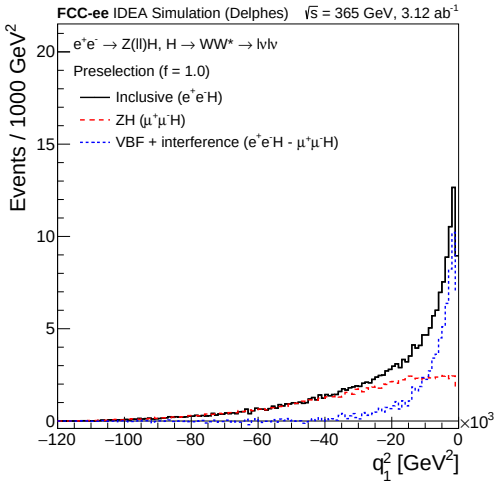
squared four-momentum transfer $|q^2|$ to peak sharply near zero.[3] In contrast, the Z-candidate leptons in the Higgsstrahlung process originate from the decay of a massive, on-shell Z boson. When the t-channel $|q^2|$ formula is evaluated using these decay products, the resulting value loses its physical interpretation as a four-momentum transfer. Instead, it acts as a purely kinematic projection governed by the Z boson mass and decay angles, which naturally yields a broad, unpeaked distribution.

The same forward-scattering topology motivates the acollinearity variable. Since the outgoing electron and positron generally follow the two oppositely directed beams, their opening angle remains close to π, giving small α_{acol} values. In Higgsstrahlung, the reconstructed Z boson is produced in the central region of the detector with substantial momentum, leading on average to larger acollinearity.

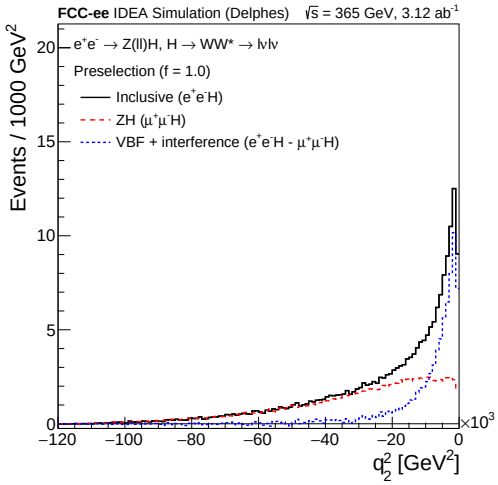
The transverse-momentum observables provide complementary information. Forward VBF electrons typically carry relatively little transverse momentum, so both individual Z-candidate lepton momenta, $p_{\text{T}}^{\ell_{Z1}}$ and $p_{\text{T}}^{\ell_{Z2}}$, and their vector-sum magnitude, $p_{\text{T}}^{\ell\ell}$, tend to populate lower values. In the two-body Higgsstrahlung process, the Z boson recoils against the Higgs boson and can acquire substantial transverse momentum; its decay leptons and the reconstructed dilepton system therefore generally have harder p_{T} spectra. Requirements rejecting the low-$|q^2|$, low-α_{acol}, and low-p_{T} regions are thus considered as possible VBF suppressors.

The distributions before the optimized selections are collected in Figure 16, and the distributions after the full event selection are shown in Figure 17. Ultimately, none of these additional variables are required. Since the $f = 1.0$ pairing metric so effectively pushes the VBF spectrum to higher dilepton masses, the application of a standard invariant mass window cut, requiring $71 < m_{\ell\ell} < 111$ GeV, proves to be the most powerful discriminator, as illustrated in Figure 14b. Under the optimized $f = 1.0$ pairing, the dilepton mass cut eliminates 95% of the ZZ-fusion-plus-interference component while retaining the vast majority of the ZH signal with 89% signal efficiency, making the other VBF suppression variables redundant.

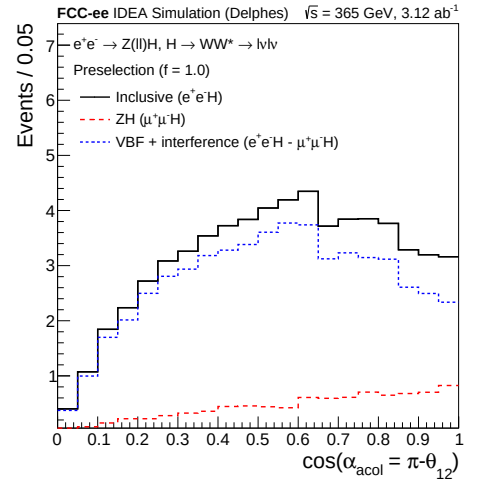
[3] In the limit of negligible electron mass, the squared four-momentum transfer is given by $q^2 = (p_{\text{beam}} - p_{\text{out}})^2 \approx -2E_{\text{beam}}E_{\text{out}}(1 - \cos\theta)$, where θ is the scattering angle relative to the beam axis. Because VBF electrons scatter in the extreme forward direction ($\theta \ll 1$), we can apply the small-angle approximation $(1 - \cos\theta) \approx \theta^2/2$. This quadratic dependence on the scattering angle strongly suppresses the magnitude of $|q^2|$, causing it to peak sharply near zero.



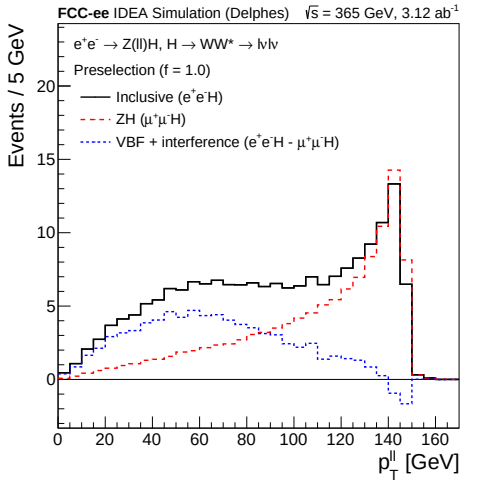
(a) Momentum transfer, q_1^2



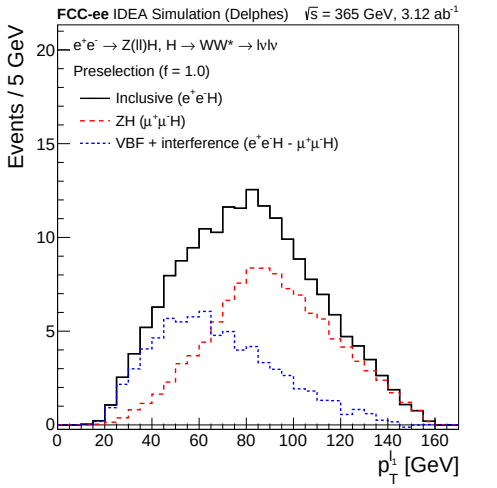
(b) Momentum transfer, q_2^2



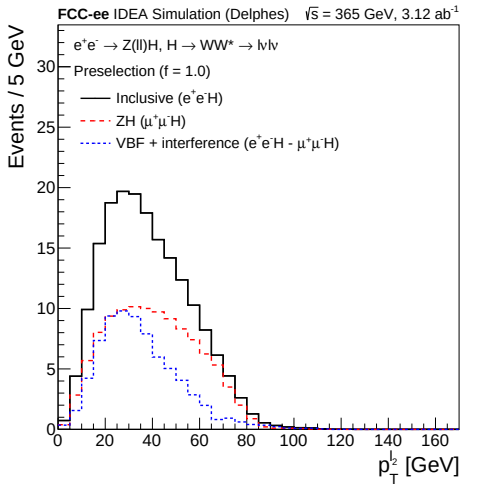
(c) Cosine of dilepton acollinearity



(d) Dilepton transverse momentum

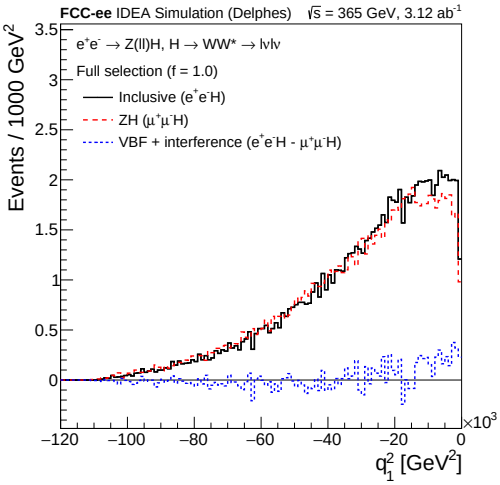


(e) Leading Z-candidate lepton p_{T}

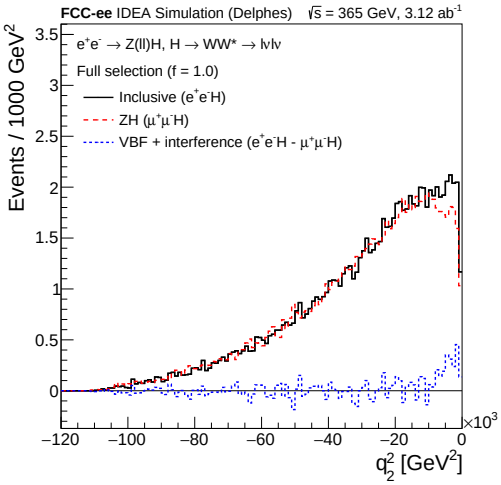


(f) Subleading Z-candidate lepton p_{T}

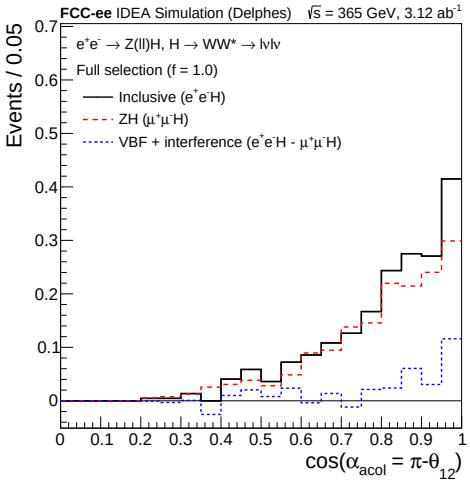
Figure 16: Distributions of the variables examined for suppressing the ZZ-fusion-plus-interference component at $\sqrt{s} = 365$ GeV, shown before the optimized kinematic selections.



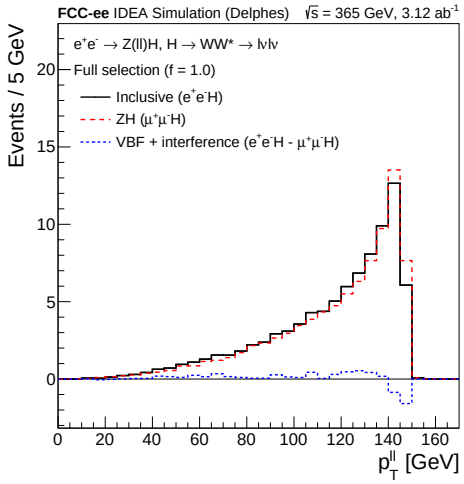
(a) Momentum transfer, q_1^2



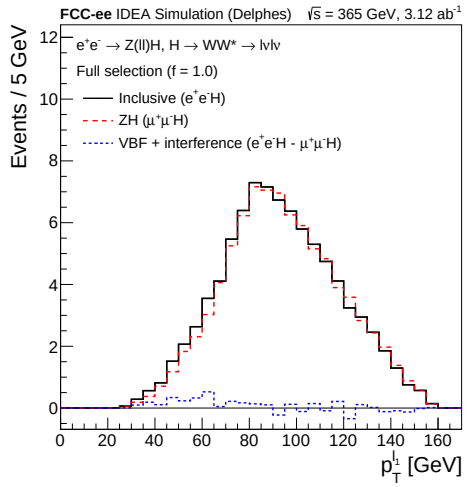
(b) Momentum transfer, q_2^2



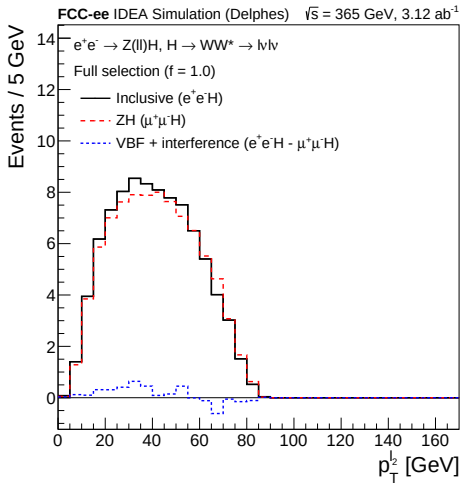
(c) Cosine of dilepton acollinearity



(d) Dilepton p_{T}



(e) Leading Z-candidate lepton p_{T}



(f) Subleading Z-candidate lepton p_{T}

Figure 17: Distributions of the VBF-suppression variables at $\sqrt{s}$ = 365 GeV after the full event selection, showing similar trends between the inclusive (black) and the ZH (red) components.

E Supplementary kinematic distributions

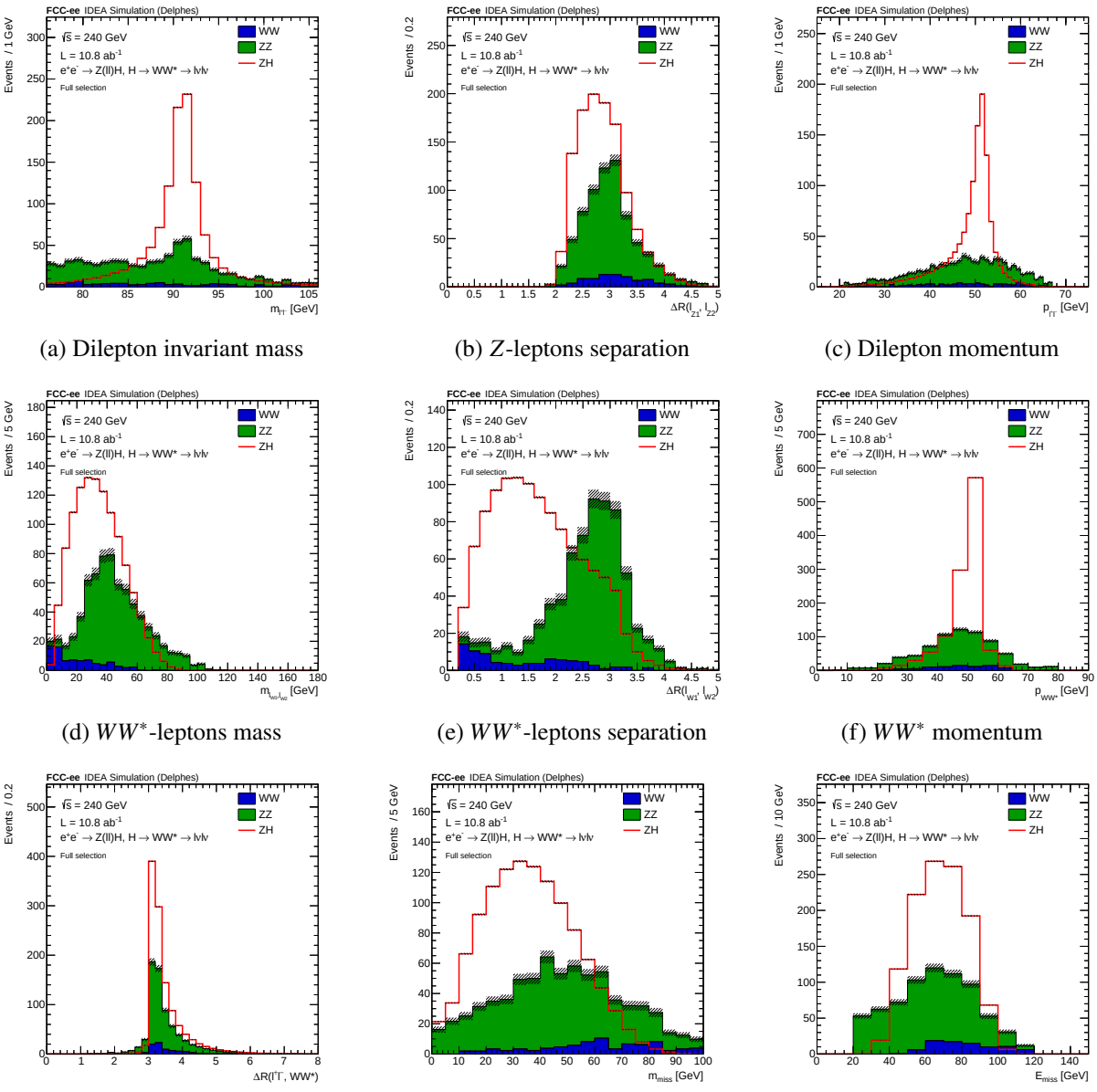
This appendix presents additional kinematic distributions for events passing the full optimized selection at the two centre-of-mass energies. They are used to illustrate the characteristic kinematics of the selected signal and surviving backgrounds and to support the comparisons discussed below.

At $\sqrt{s} = 240$ GeV, the reconstructed dilepton mass $m_{\ell\ell}$ distribution also exhibits an asymmetric shape, in addition to those observed in the m_{rec} and WW^* system mass distributions discussed in Section 7. As shown in Figure 18a, while the signal peaks sharply at the nominal Z boson mass, a noticeable tail extends toward lower mass values. This low-mass tail is primarily induced by final-state radiation (FSR): when a Z-candidate lepton radiates a photon that is not fully captured or recombined with the corresponding lepton during event reconstruction, the measured momentum of the latter is reduced. Consequently, the invariant mass calculated from the lepton pair falls below the true mass of the resonant Z boson.

The kinematic shapes of the signal at $\sqrt{s} = 365$ GeV undergo a fundamental shift driven by the higher collision energy. At 240 GeV, Higgsstrahlung occurs relatively close to the ZH production threshold, and the Z and Higgs bosons therefore have substantially smaller momenta than at 365 GeV. Consequently, the Z-candidate leptons are pushed to significantly higher momenta, as seen in Figure 21 compared with Figure 20. The corresponding increase in the absolute momentum uncertainty (which grows roughly as p_{T}^2) is expected to contribute to the broader reconstructed Z-candidate mass distribution at 365 GeV. In the muon channel, the efficiency of the $m_{\ell\ell}$ requirement decreases from approximately 94% for $76 < m_{\ell\ell} < 106$ GeV at 240 GeV to 89% for the wider $71 < m_{\ell\ell} < 111$ GeV window at 365 GeV. This difference is consistent with the observed broadening. In the electron channel, the nonresonant ZZ-fusion contribution and its interference with Higgsstrahlung further broaden and distort the inclusive $m_{\ell\ell}$ distribution.

Furthermore, the higher-energy collision consequently produces more strongly boosted Z and Higgs bosons, such that the final-state particles become more collimated. This manifests as a smaller angular separation between the two leptons of the Z-candidate (Figure 19b), as well as between the two leptons originating from the W decays (Figure 19e).

In contrast, the angular separation between the reconstructed Z and WW^* systems changes relatively little between the two energies, as seen in Figures 18g and 19g. This reflects the approximately back-to-back topology of the Born-level $e^+e^- \to ZH$ process. Their azimuthal separation is close to π, while $\Delta R(Z \to \ell\ell, WW^*)$ also includes their pseudorapidity separation and can therefore extend above π.

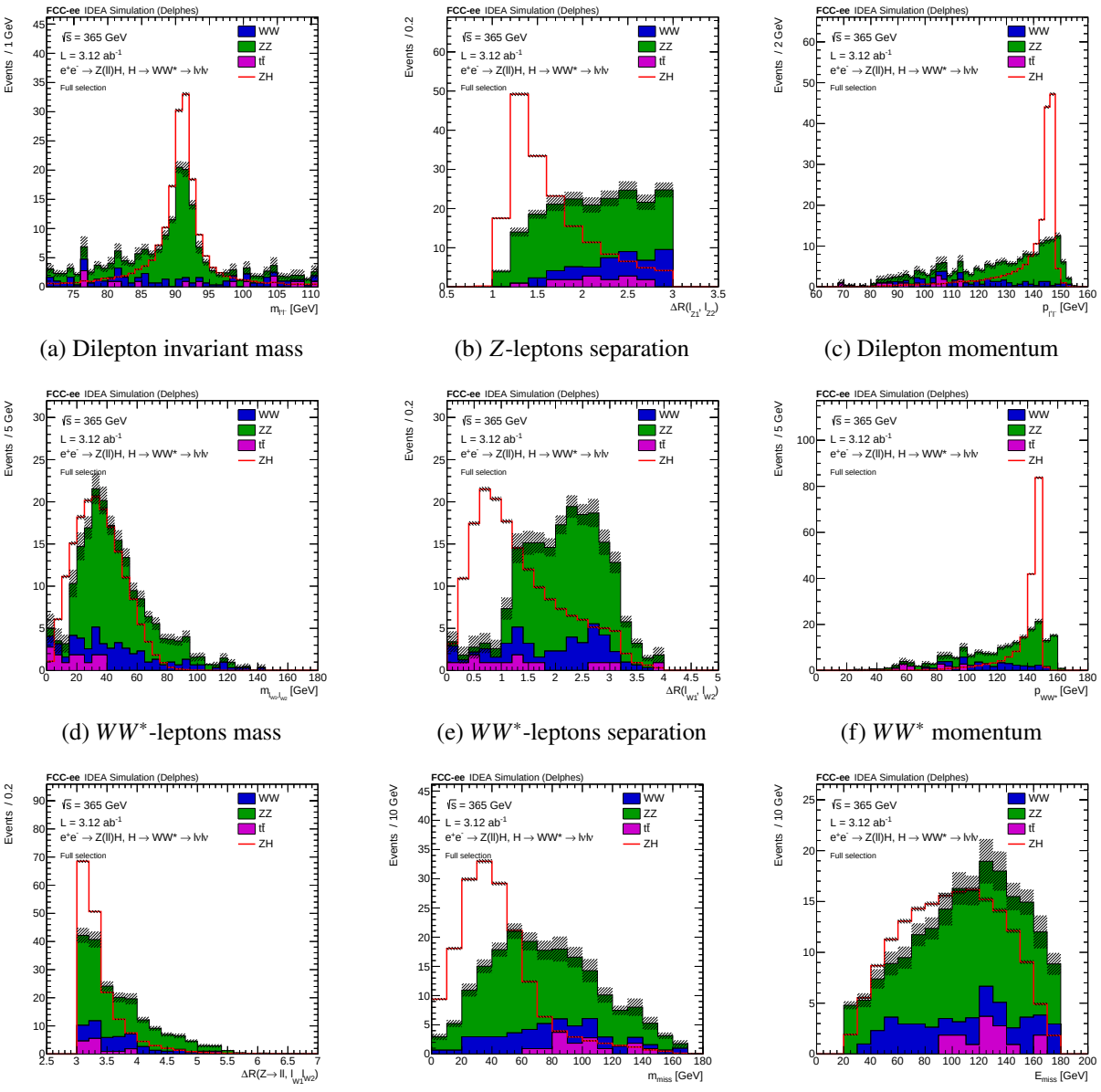


(a) Dilepton invariant mass (b) Z-leptons separation (c) Dilepton momentum

(d) WW^*-leptons mass (e) WW^*-leptons separation (f) WW^* momentum

(g) Systems separation (h) Missing mass (i) Missing energy

Figure 18: Selected BDT input-feature distributions at $\sqrt{s} = 240$ GeV after the full event selection.

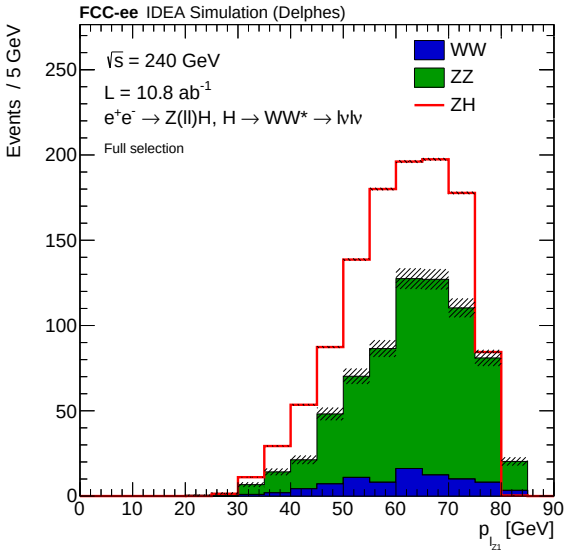


(a) Dilepton invariant mass (b) Z-leptons separation (c) Dilepton momentum

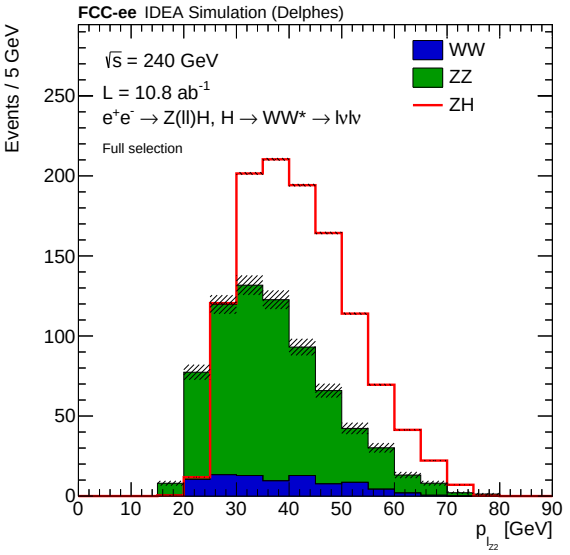
(d) WW^*-leptons mass (e) WW^*-leptons separation (f) WW^* momentum

(g) Systems separation (h) Missing mass (i) Missing energy

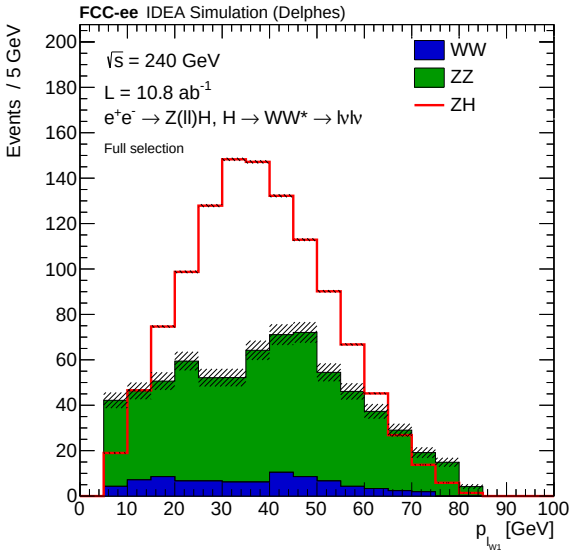
Figure 19: Selected BDT input-feature distributions at $\sqrt{s} = 365$ GeV after the full event selection.



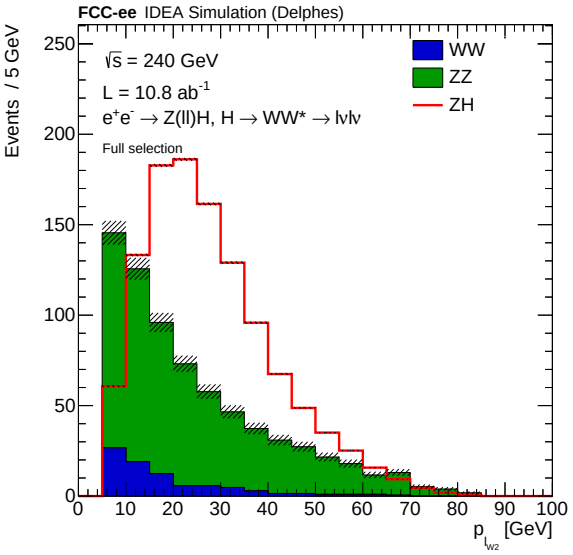
(a) Leading Z-candidate lepton, $p_{\ell_{Z1}}$



(b) Subleading Z-candidate lepton, $p_{\ell_{Z2}}$

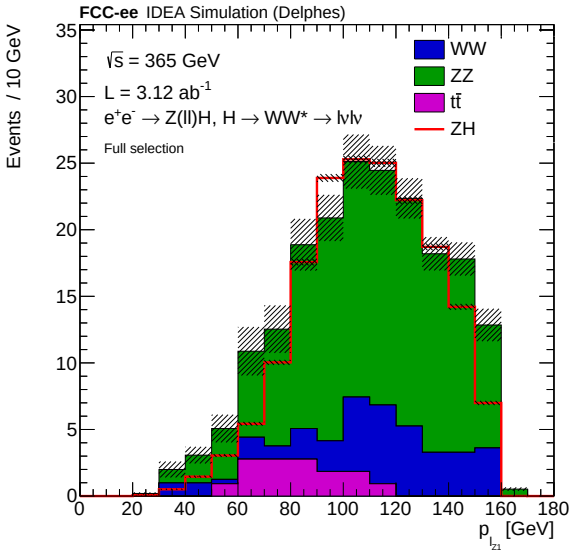


(c) Leading W-candidate lepton, $p_{\ell_{W1}}$

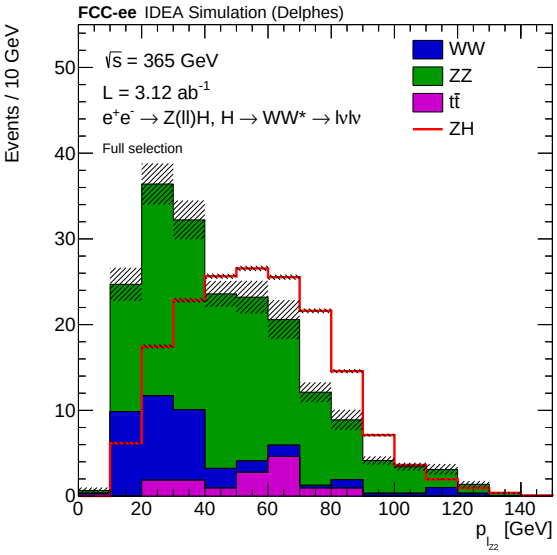


(d) Subleading W-candidate lepton, $p_{\ell_{W2}}$

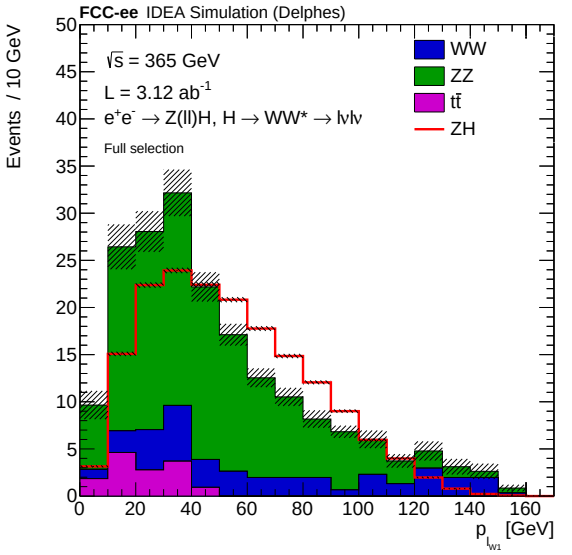
Figure 20: Momentum distributions of the individual Z- and W-candidate leptons at $\sqrt{s} = 240$ GeV after the full event selection.



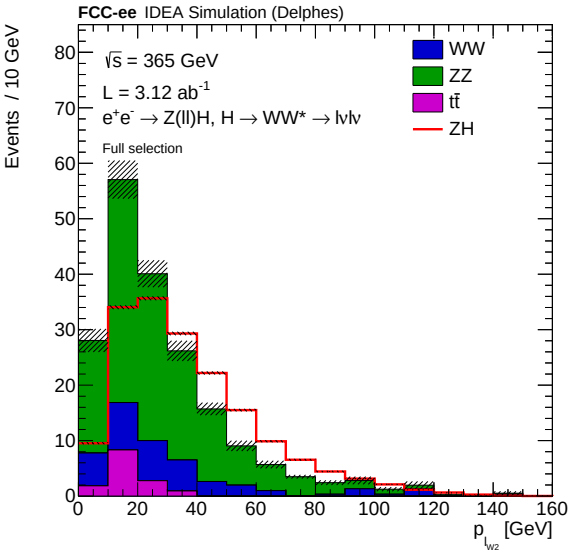
(a) Leading Z-candidate lepton, $p_{\ell_{Z1}}$



(b) Subleading Z-candidate lepton, $p_{\ell_{Z2}}$



(c) Leading W-candidate lepton, $p_{\ell_{W1}}$



(d) Subleading W-candidate lepton, $p_{\ell_{W2}}$

Figure 21: Momentum distributions of the individual Z- and W-candidate leptons at $\sqrt{s} = 365$ GeV after the full event selection.

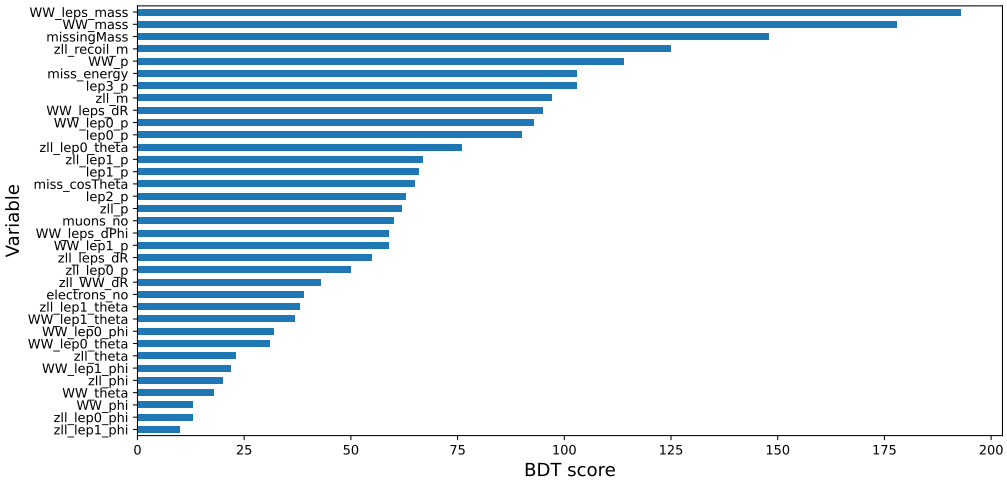
F BDT-based classification training and validation

Independent BDT models are trained for the $\sqrt{s}$ = 240 and 365 GeV operating points using the same configuration. The dedicated training samples are statistically independent of the Monte Carlo samples used in the final analysis. Because of the limited available WW and $t\bar{t}$ simulation, only the dominant ZZ process is used as the background during training. The 240 GeV dataset contains approximately 26,000 unweighted signal events and 1,800 unweighted ZZ events, while the 365 GeV dataset contains approximately 60,000 signal and 130,000 ZZ events. Each dataset is randomly divided into 70% for training, 20% for validation, and 10% for testing.

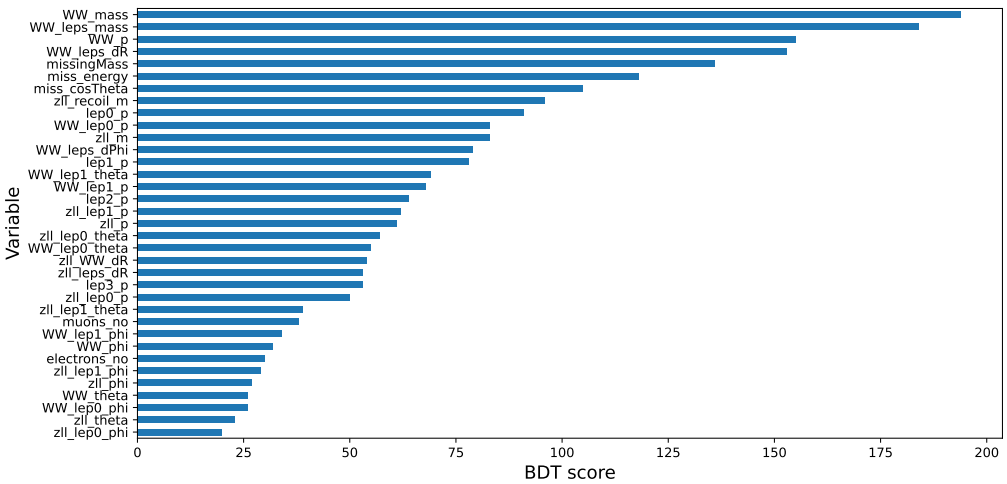
The models are implemented with XGBoost [27] using a binary logistic objective. Binary cross-entropy is minimized during training, and a sigmoid transformation maps the classifier response to a continuous score between zero and one. The hyperparameters comprise a maximum tree depth of 5, a learning rate of 0.20, and at most 350 estimators. Early stopping based on the validation sample is used to limit overtraining.

The classifiers use the full set of reconstructed event-level kinematic observables, listed in Table 5. Figure 22 shows their relative feature importance. At both energies, m_{WW^*} and $m_{\ell_{W1}\ell_{W2}}$ provide the greatest discriminating power, with their ordering reversed between 240 and 365 GeV.

The classifier performance for 365 GeV is shown in Figure 23, while the corresponding plots for 240 GeV are shown in Figure 7. The agreement between the training and testing score distributions indicates no significant overtraining. Both classifiers achieve an AUC of approximately 99%.

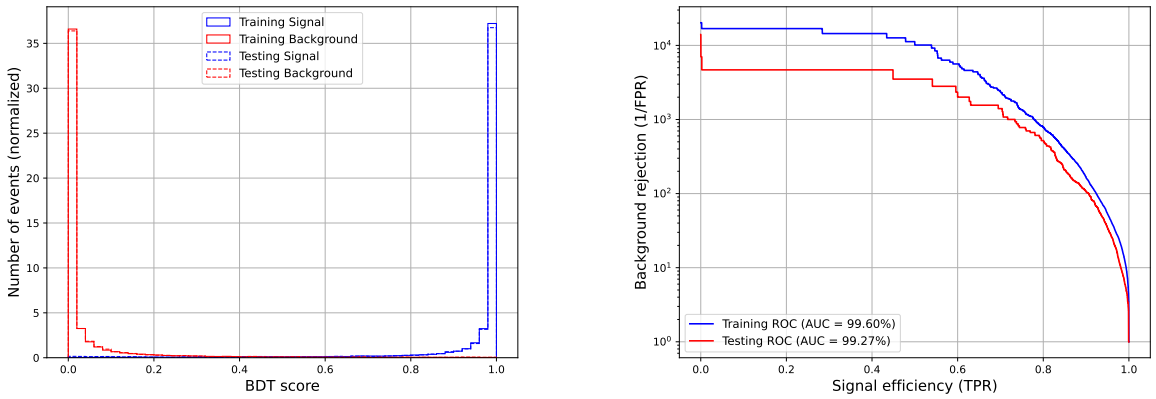


(a) $\sqrt{s}$ = 240 GeV



(b) $\sqrt{s}$ = 365 GeV

Figure 22: Relative importance of the input features used by the BDT classifiers at the two centre-of-mass energies.



(a) Training and testing score distributions

(b) Background rejection versus signal efficiency

Figure 23: Performance of the BDT-based classifier at $\sqrt{s} = 365$ GeV. The background rejection in the right panel is defined as the inverse of the background efficiency. The corresponding plots for the $\sqrt{s} = 240$ GeV classifier are shown in Figure 7.